NOAA Technical Report ERL 429–WPL 60

Data Analysis of the NOAA-GIT Millimeter-Wave Propagation Experiment Near Flatville, Illinois

R. J. Hill, W. P. Schoenfeld,
J. P. Riley, J. T. Priestley,
S. F. Clifford, S. P. Eckes,
R. A. Bohlander, R. W. McMillan

August 1985

U.S. DEPARTMENT OF COMMERCE
National Oceanic and Atmospheric Administration
Environmental Research Laboratories

NOAA Technical Report ERL 429–WPL 60

Data Analysis of the NOAA-GIT Millimeter-Wave Propagation Experiment Near Flatville, Illinois

R. J. Hill, W. P. Schoenfeld,
J. P. Riley, J. T. Priestley,
S. F. Clifford, S. P. Eckes,
R. A. Bohlander, R. W. McMillan

Wave Propagation Laboratory
Boulder, Colorado

August 1985

U.S. DEPARTMENT OF COMMERCE
Malcolm Baldrige, Secretary

National Oceanic and Atmospheric Administration

Environmental Research Laboratories
Boulder, Colorado
Vernon E. Derr, Director

NOTICE

Mention of a commercial company or product does not constitute an endorsement by NOAA Environmental Research Laboratories. NOAA does not authorize any use of information from this publication for advertising or publicity purposes.

CONTENTS

		Page
ABSTRACT		1
1.	INTRODUCTION	1
2.	QUANTITIES COMPUTED FROM THE GIT MILLIMETER-WAVE DATA	2
	2.1 Introduction	2
	2.2 Phase-Difference Statistics	4
	2.3 Intensity Statistics	5
	2.4 Mixed Intensity and Phase-Difference Statistics	6
	2.5 Second Moment of the Field: The Mutual Coherence Function	7
	2.6 Fourth Moment of the Field	9
	2.7 Extrema	13
	2.8 Probability Distribution Functions	13
	2.9 Fourier Transforms	13
	2.10 Figures of Merit	14
3.	QUANTITIES COMPUTED FROM THE NOAA MICROMETEOROLOGICAL DATA	15
	3.1 Introduction	15
	3.2 Conversion to Units	17
	3.3 Averages, Variances, and Cross-Correlations	19
	3.4 Turbulence Fluxes	20
	3.5 Spatial Structure Parameters	22
	3.6 Time-Lagged Structure Parameters	23
	3.7 Extrema	24
	3.8 Probability Distribution Functions	24
	3.9 Fourier Transforms	25
	3.10 Refraction and Absorption Structure Parameters	25
4.	PROBLEMS WITHIN THE DATA	27
	4.1 Introduction	27
	4.2 Cures for Data Aquisition Errors	27
	4.3 Cures for Millimeter-Wave Data Problems	28
	4.4 Cures for Micrometeorological Data Problems	31
5.	OVERVIEW OF THE DATA PROCESSING SOFTWARE	34
	5.1 Introduction	34
	5.2 FLATCOPY	36
	5.3 METAPE	37
	5.4 Stripchart Data Visualization	38
	5.5 PED 2 PAR and MODPARM	40
	5.6 MILDRV and METDRV	41
	5.7 Graphing the 25.6 s Statistics	42
	5.8 MILRDR and METRDR	43
	5.9 MILFFT and METFFT	44
	5.10 Using the Answer Files	45
	5.11 Archiving of Disk Files	46

6. REDUCED MILLIMETER-WAVE AND MICROMETEOROLOGICAL DATA..... 46

6.1 Introduction..... 46
6.2 Tabular Results..... 47
6.3 Graphical Results..... 50

7. ACKNOWLEDGMENTS..... 54

8. REFERENCES..... 54

Data Analysis of the NOAA-GIT Millimeter-Wave Propagation Experiment Near Flatville, Illinois

R. J. Hill, W. P. Schoenfeld[1], J. P. Riley, J. T. Priestley,
S. F. Clifford, S. P. Eckes[1], R. A. Bohlander[2], R. W. McMillan[2]

ABSTRACT. The authors discuss the quantities calculated from the millimeter-wave and micrometorological data base. The data base was obtained from the millimeter-wave propagation experiment conducted near Flatville, Illinois, by the National Oceanic and Atmospheric Administration (NOAA) and Georgia Institute of Technology (GIT). The repair of data-base errors by digital computation is also discussed, and the overall structure of the data-processing programming is described.

1. INTRODUCTION

The millimeter-wave propagation experiment consisted of five data-taking sessions. The dates for these sessions, including on-site setup and takedown, were June 3 to July 15, 1983; October 30 to December 11, 1983; February 5 to March 9, 1984; May 29 to July 5, 1984; and January 29 to March 26, 1985. Figure 1 is a self-explanatory diagram of the experiment. Georgia Institute of Technology (GIT) was responsible for the millimeter-wave data, and the National Oceanic and Atmospheric Administration (NOAA) for the micrometeorological data. The methods of analysis for the clear-air portion of the micrometeorological data are described here; analyses of the meteorological data for fog, rain, and snow are not discussed. On the other hand, the methods of analysis for the millimeter-wave data given here are identical for clear air, fog, rain, or snow.

---

[1]Cooperative Institute for Research in Environmental Sciences, University of Colorado and National Oceanic and Atmospheric Administration, Boulder, CO 80309.

[2]Engineering Experiment Station, Georgia Institute of Technology, Atlanta, GA 30332.

The philosophy underlying the data processing is as follows. We calculate all quantities of interest using as few computer programs as possible. For instance, we avoid programming that has the special purpose of calculating intensity covariance or the mutual coherence function. All such diverse statistics are calculated through one program, thereby reducing the complexity of the program library and reducing input/output costs. We use visual inspection of the data from computer-generated microfilm stripcharts that reveal full data time series. Quantities are also averaged into time intervals of 2.56 and 25.6 s and graphed to reveal trends and other problems. We examine graphs of power spectra and cross-spectra to detect noise in the data. Only by such means of data visualization can we be sure that the myriad errors within the data can be identified and avoided. This visualization of the data is thus essential to our data validation. Finally, the end product of the data analysis programs is what we call answer files that contain the statistics from statistically stationary periods on each data tape. Thus investigators are not limited in their interpretation of the data by any a priori decisions as to how the results are to be presented. For instance, the answer files may be interrogated to produce plots of the mutual coherence function for a variety of surface-layer stabilities, each stability case arising from different data runs. There remains great flexibility in graphing and tabulating the answer files for the purpose of making scientific discoveries. Investigators are then limited only by their insight and ingenuity.

2. QUANTITIES COMPUTED FROM THE GIT MILLIMETER-WAVE DATA

2.1 Introduction

The GIT millimeter-wave data consist of 28 channels taken at 100 Hz. (In this report "millimeter-wave" is abbreviated as mm-wave.) Figure 1 shows the arrangement of receiver antennas, housed in a trailer, as viewed from the transmitter; the antennas are designated by a number. There are six possible antenna pairs, each with a different spacing. The antenna pair numbers and their spacings are given in Table 1. For a few experiment runs, the fifth antenna, below antenna 2 (see Fig. 1), was used in place of antenna 4; the objective was observation of anisotropy or multipath effects.

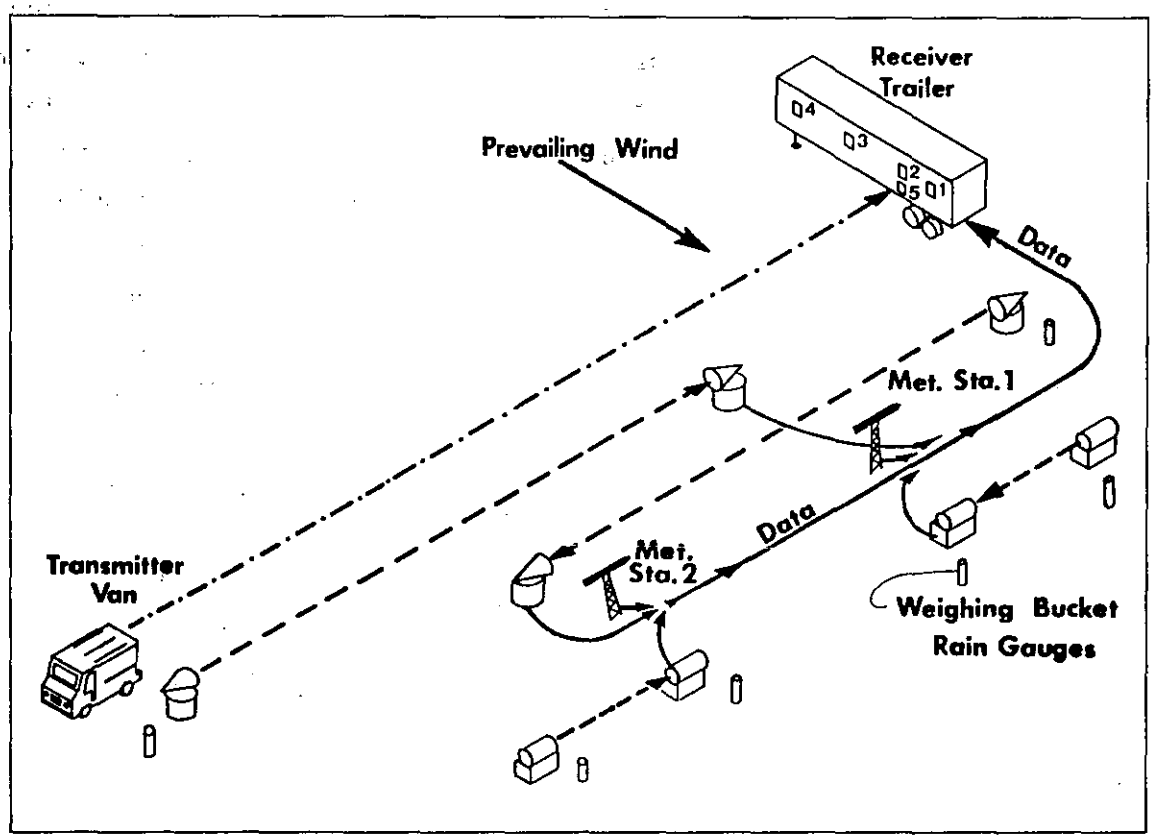

Figure 1.--The instrument positions at the experiment site. The dashed and dotted line denotes mm-wave propagation path (1.4 km); the long-dashed lines, the optical propagation paths (1 km each); and the short-dashed lines, the optical rain gauge paths (50 m each). Solid lines show the flow of micrometeorological data to the data aquisition system in the receiver trailer. Antennas are numbered 1 to 5 in the receiver trailer.

Table 1.--Antenna pairs

Pair number	Antenna pair	Spacing in meters
1	1 & 2	1.43
2	1 & 3	4.29
3	1 & 4	10.00
4	2 & 3	2.86
5	2 & 4	8.57
6	3 & 4	5.71

For each antenna pair, the GIT mm-wave data contain the square of the voltage from four phase shifts of 0°, 90°, 180°, and 270°. For the antenna pair formed by antennas i and j these are denoted by

$$(V_0)^2_{ij} \text{ , } (V_{90})^2_{ij} \text{ , } (V_{180})^2_{ij} \text{ , and } (V_{270})^2_{ij} \text{ .} \qquad (1)$$

The data also contain the intensity at each antenna, denoted by I_i for the ith antenna.

It is important to keep in mind that the intensities are measured in arbitrary units and that differences exist between the time-averaged (hereafter referred to as mean) intensities of different antennas. Thus any statistics calculated from the intensities must be normalized by the appropriate mean intensities. Because of hardware characteristics, the phase difference between antenna pairs has an arbitrary offset that is different for each pair. Thus any phase-difference statistics must be calculated from the phase difference with its mean value subtracted.

Drift in the mm-wave receivers causes the measured intensities and squared voltages in (1) to change slowly with time. Thus it is necessary to low-pass filter the mm-wave data; the filter frequency can be varied as needed. We redefine the phase difference as its value with its low-pass-filtered value subtracted. To excellent approximation, the mean phase difference is then zero. We redefine the intensity as its value divided by its low-pass-filtered value. Then, to excellent approximation, the mean intensity is unity. In the following we discuss various statistical quantities for which mean phase differences are subtracted and mean intensities are divided out. One must keep in mind that if the low-pass filtering is used, then a subsequent subtraction of the mean phase difference and scaling by the mean intensity has essentially no effect. However, if the low-pass filtering is not used, then the computer code continues to operate correctly by subtracting the nontrivial mean phase difference, and scaling by the nonunity mean intensities.

2.2 Phase-Difference Statistics

The phase difference for antenna pair i and j is computed using the following:

$$\beta_{ij} = \arctan\left[\frac{(V_{90})^2_{ij} - (V_{270})^2_{ij}}{(V_0)^2_{ij} - (V_{180})^2_{ij}}\right] . \qquad (2)$$

The Fortran ATAN2 function is used in the computations. This gives β_{ij} in the range $-\pi$ to π. That range is extended to -2π to 2π by following the transition in the value of ATAN2 as the phase difference crosses $-\pi$ or π. It is possible to extend the range to $-\infty$ to ∞ by slightly more complicated programming; this has not been done since it is expected that the range from -2π to 2π will never be exceeded. In any case, we will be aware from microfilm stripcharts if this range is exceeded.

For each antenna pair we calculate mean phase difference $\langle\beta_{ij}\rangle$ and the mean of the squared phase difference $\langle(\beta_{ij})^2\rangle$ from which we obtain the phase-difference variance

$$\langle(\beta_{ij} - \langle\beta_{ij}\rangle)^2\rangle = \langle(\beta_{ij})^2\rangle - \langle\beta_{ij}\rangle^2 . \qquad (3)$$

These six variances produce the phase structure function, when graphed as a function of antenna spacing.

2.3 Intensity Statistics

For each antenna, we calculate the mean intensity $\langle I_i\rangle$ and the mean of the squared intensity $\langle I_i^2\rangle$. From these we obtain the normalized intensity variance

$$\sigma_i^2 = \frac{\langle(I_i - \langle I_i\rangle)^2\rangle}{\langle I_i\rangle^2} = \frac{\langle I_i^2\rangle}{\langle I_i\rangle^2} - 1 . \qquad (4)$$

For each of the antenna pairs i and j, we calculate the cross-product average $\langle I_i\ I_j\rangle$; this gives the normalized covariance

$$C_{ij} = \frac{\langle(I_i - \langle I_i\rangle)(I_j - \langle I_j\rangle)\rangle}{\sqrt{\langle(I_i - \langle I_i\rangle)^2\rangle}\ \sqrt{\langle(I_j - \langle I_j\rangle)^2\rangle}} \qquad i \neq j \qquad (5)$$

or

$$C_{ij} = \frac{\langle I_i\ I_j\rangle - \langle I_i\rangle\langle I_j\rangle}{\sigma_i\ \sigma_j\ \langle I_i\rangle\langle I_j\rangle} \ . \tag{6}$$

When graphed versus antenna spacing, the six C_{ij} are the normalized spatial covariance. On the basis of inertial-range theory and no absorption fluctuations, the minimum antenna separation of 1.43 m implies that the normalized covariance would be only about 0.1, and be very much smaller at larger separations. Thus the effects of absorption fluctuations might be seen in the large-spacing covariance values because the absorption fluctuations affect much larger spatial scales in the scintillation pattern than do refractive fluctuations.

2.4 Mixed Intensity and Phase-Difference Statistics

For each antenna pair, we calculate the intensity-phase-difference cross-correlations $\langle I_i\ \beta_{ij}\rangle$ and $\langle I_j\ \beta_{ij}\rangle$. These are used to obtain the quantity

$$\frac{1}{2}\left\langle\left(\frac{I_i}{\langle I_i\rangle} - \frac{I_j}{\langle I_j\rangle}\right)\beta_{ij}\right\rangle = \frac{1}{2}\left(\frac{\langle I_i\ \beta_{ij}\rangle}{\langle I_i\rangle} - \frac{\langle I_j\ \beta_{ij}\rangle}{\langle I_j\rangle}\right) . \tag{7}$$

We define the log-amplitude by $\chi_i \equiv \ell n(A_i/\langle A_i\rangle)$. Since

$$\langle I\rangle = \langle A^2\rangle = \langle (A - \langle A\rangle)^2\rangle + \langle A\rangle^2 \ , \tag{8}$$

and for our case of weak scintillation the amplitude variance is much smaller than the square of the mean amplitude, then $\langle I\rangle \simeq \langle A\rangle^2$. So the log-amplitude can be approximated by

$$\chi_i \simeq \frac{1}{2}\ \ell n(I_i/\langle I_i\rangle) \tag{9}$$

$$= \frac{1}{2}\ \ell n\left(1 + \frac{I_i - \langle I_i\rangle}{\langle I_i\rangle}\right) \tag{10}$$

$$= \frac{1}{2}\left[\frac{I_i - \langle I_i\rangle}{\langle I_i\rangle} - \frac{1}{2}\left(\frac{I_i - \langle I_i\rangle}{\langle I_i\rangle}\right)^2 + \cdots\right] . \tag{11}$$

Therefore, to first order in the smallness of intensity fluctuations relative to their mean, which is an excellent approximation, we have the quantity

$$\langle(\chi_i - \chi_j)\ \beta_{ij}\rangle \approx \frac{1}{2}\left\langle\left(\frac{I_i}{\langle I_i\rangle} - \frac{I_j}{\langle I_j\rangle}\right)\beta_{ij}\right\rangle . \tag{12}$$

2.5 Second Moment of the Field: The Mutual Coherence Function

Let U_i denote the electromagnetic field at the ith antenna, and let U_j^* denote the field's complex conjugate at antenna j. The second moment of the field, known as the mutual coherence function, MCF, is $\langle U_i\ U_j^*\rangle$. We do not calculate the case i = j because $\langle U_i\ U_i^*\rangle = \langle I_i\rangle$ is the average intensity, which is already calculated as in Sec. 2.3. If we write the field as

$$U_i = A_i e^{i\phi_i} \tag{13}$$

where $A_i = \sqrt{I_i}$ is its amplitude and ϕ_i is its phase, then the MCF is

$$\langle U_i\ U_j^*\rangle = \langle A_i\ A_j\ e^{i(\phi_i - \phi_j)}\rangle \tag{14}$$

$$= \langle A_i\ A_j\ e^{i(\beta_{ij} - \langle\beta_{ij}\rangle)}\rangle . \tag{15}$$

Here the phase difference is

$$\phi_i - \phi_j = \beta_{ij} - \langle\beta_{ij}\rangle , \tag{16}$$

since β_{ij} from Eq. (2) is the phase difference to within an arbitrary offset, this offset being removed by subtracting $\langle\beta_{ij}\rangle$. The unnormalized MCF is not meaningful because the intensities are known only in arbitrary units. The normalized MCF is denoted by M_2 and is given by

$$M_2 = \frac{\langle U_i\ U_j^*\rangle}{\sqrt{\langle U_i\ U_i^*\rangle\langle U_j\ U_j^*\rangle}} \tag{17}$$

or

$$M_2 = \frac{\langle \sqrt{I_i\ I_j}\ e^{i\beta_{ij}} \rangle}{\sqrt{\langle I_i \rangle \langle I_j \rangle}\ e^{i\langle \beta_{ij} \rangle}} \quad . \tag{18}$$

We use the relationship

$$e^{i\beta_{ij}} = \cos(\beta_{ij}) + i \sin(\beta_{ij}) \quad . \tag{19}$$

We then average the real and imaginary parts of the numerator of M_2; namely, we calculate the averages of R_{ij} and J_{ij} where

$$R_{ij} \equiv \sqrt{I_i\ I_j} \cos(\beta_{ij}) \tag{20}$$

$$J_{ij} \equiv \sqrt{I_i\ I_j} \sin(\beta_{ij}) \quad . \tag{21}$$

Note that we must take the sine and cosine of β_{ij}, which itself is an arctangent, rather than using identities for trignometric functions of the arctangent because we must use a temporal filter on β_{ij} (see Sec. 4.3) but we must not filter the quantities in (1). The inverse of the denominator of M_2 can be written as $R_D - iJ_D$, where

$$R_D = \cos(\langle \beta_{ij} \rangle) / \sqrt{\langle I_i \rangle \langle I_j \rangle} \tag{22}$$

$$J_D = \sin(\langle \beta_{ij} \rangle) / \sqrt{\langle I_i \rangle \langle I_j \rangle} \quad , \tag{23}$$

so

$$M_2 = (\langle R_{ij} \rangle + i\langle J_{ij} \rangle)(R_D - iJ_D) \quad . \tag{24}$$

The normalization of the MCF is performed in real arithmetic; the real and imaginary parts of M_2 are determined from

$$\mathrm{Re}(M_2) = \langle R_{ij} \rangle R_D + \langle J_{ij} \rangle J_D \tag{25}$$

$$\mathrm{Im}(M_2) = \langle J_{ij} \rangle R_D - \langle R_{ij} \rangle J_D \quad . \tag{26}$$

The modulus and phase of M_2 are also calculated using

$$r = \{[\mathrm{Re}(M_2)]^2 + [\mathrm{Im}(M_2)]^2\}^{1/2} \tag{27}$$

$$\Phi = \arctan[\mathrm{Im}(M_2)/\mathrm{Re}(M_2)] \tag{28}$$

such that

$$M_2 = r\, e^{i\Phi} \quad . \tag{29}$$

2.6 Fourth Moment of the Field

Having four receiving antennas allows us to calculate the fourth moment of the field, which is given by

$$\langle U_i\, U_j^*\, U_n\, U_m^* \rangle \quad .$$

If $i = j = n = m$ then $M_4 = \langle I_i^{\,2} \rangle$, which is the mean of the squared intensity and has been calculated in Sec. 2.3. If, for instance, $i = j$ and $n = m$, then the fourth moment becomes $\langle I_i\, I_n \rangle$, which has also been calculated in Sec. 2.3. Thus, not all possible combinations of i, j, n, and m are of interest. In fact, certain choices of i, j, n, and m merely produce the complex conjugate fourth moment arising from a different choice of indexes or produces the same fourth moment because of multiplicative commutation. Thus we calculate only those fourth moments that are distinct from intensity products and are distinct under complex conjugation and multiplicative commutation. The sets of i, j, n, m that produce these distinct values of M_4 are given in Table 2.

Similar to the case of the second moment of the field, only the normalized fourth moment is meaningful because the intensities are known only in

Table 2.--Indexes for producing distinct values of M_4

Case	i	j	n	m
1	1	2	3	4
2	1	2	4	3
3	1	3	2	4
4	1	1	1	2
5	1	1	1	3
6	1	1	1	4
7	1	1	2	3
8	1	1	2	4
9	1	1	3	4
10	2	2	1	2
11	2	2	1	3
12	2	2	1	4
13	2	2	2	3
14	2	2	2	4
15	2	2	3	4
16	3	3	1	2
17	3	3	1	3
18	3	3	1	4
19	3	3	2	3
20	3	3	2	4
21	3	3	3	4
22	4	4	1	2
23	4	4	1	3
24	4	4	1	4
25	4	4	2	3
26	4	4	2	4
27	4	4	3	4
28	1	2	1	2
29	1	3	1	3
30	1	4	1	4
31	2	3	2	3
32	2	4	2	4
33	3	4	3	4

arbitrary units and the phase differences are known only to within additive constants. The normalized fourth moment is defined by

$$M_4 = \frac{\langle U_i U_j^* U_n U_m^* \rangle}{\sqrt{\langle U_i U_i^* \rangle \langle U_j U_j^* \rangle \langle U_n U_n^* \rangle \langle U_m U_m^* \rangle}} \quad . \tag{30}$$

By analogy with the second moment, this gives

$$M_4 = \frac{\langle \sqrt{I_i\ I_j\ I_n\ I_m}\ \exp[i(\beta_{ij} + \beta_{nm})] \rangle}{\sqrt{\langle I_i \rangle \langle I_j \rangle \langle I_n \rangle \langle I_m \rangle}\ \exp[i(\langle \beta_{ij} \rangle + \langle \beta_{nm} \rangle)]} . \tag{31}$$

In the computation we average the real and imaginary parts of the numerator of M_4; namely, we obtain the averages $\langle R_4 \rangle$ and $\langle J_4 \rangle$ where

$$\langle R_4 \rangle \equiv \langle \sqrt{I_i\ I_j\ I_n\ I_m}\ \cos(\beta_{ij} + \beta_{nm}) \rangle \tag{32}$$

$$\langle J_4 \rangle \equiv \langle \sqrt{I_i\ I_j\ I_n\ I_m}\ \sin(\beta_{ij} + \beta_{nm}) \rangle . \tag{33}$$

For the first case in Table 2, R_4 and J_4 are calculated by noting that

$$R_4 = R_{12}\ R_{34} - J_{12}\ J_{34} \tag{34}$$

$$J_4 = J_{12}\ R_{34} + R_{12}\ J_{34} \tag{35}$$

where R_{ij} and J_{ij} were previously calculated values of the real and imaginary parts of the instantaneous second moment and are given in Eqs. (20) and (21). The second and third cases in Table 2 are calculated similarly. Cases 4 to 27 in Table 2 have one pair of equal indexes, i = j. These are calculated by noting that

$$R_4 = I_i\ R_{nm} \tag{36}$$

$$J_4 = I_i\ J_{nm} \tag{37}$$

where I_i is the intensity at antenna i (and also j since i = j); R_{nm} and J_{nm} are the real and imaginary parts of the instantaneous second moment for the remaining antenna pair as given in Eqs. (20) and (21). Finally, cases 28 to 33 in Table 2 are the squares of instantaneous second moments (since

n = i and m = j) and are thus calculated using

$$R_4 = (R_{ij})^2 - (J_{ij})^2 \tag{38}$$

$$J_4 = 2\, R_{ij}\, J_{ij} \,. \tag{39}$$

The inverse of the denominator of M_4 can be written as $R_{4D} - iJ_{4D}$, where

$$R_{4D} \equiv \cos(\langle\beta_{ij}\rangle + \langle\beta_{nm}\rangle)/d \tag{40}$$

$$J_{4D} \equiv \sin(\langle\beta_{ij}\rangle + \langle\beta_{nm}\rangle)/d \,. \tag{41}$$

Here

$$d = \sqrt{\langle I_i\rangle\, \langle I_j\rangle\, \langle I_n\rangle\, \langle I_m\rangle} \,, \tag{42}$$

so

$$M_4 = (\langle R_4\rangle + i\langle J_4\rangle)(R_{4D} - iJ_{4D}) \,. \tag{43}$$

For cases 1 to 3 in Table 2 these definitions of R_{4D} and J_{4D} are used literally. For cases 4 to 27, in which i = j, we have $\beta_{ij} = 0$ and $I_i = I_j$, so the following simplified expressions are used:

$$R_{4D} = \cos(\langle\beta_{nm}\rangle)/d \tag{44}$$

$$J_{4D} = \sin(\langle\beta_{nm}\rangle)/d \tag{45}$$

with $d = \langle I_i\rangle \sqrt{\langle I_n\rangle\, \langle I_m\rangle}$. These trigonometric evaluations and the square root in d are the same as were used in normalizing the second moment, so they need not be computed a second time. For cases 28 to 33 in Table 2, in which i = j and n = m, we use

$$R_{4D} = R_D^{\,2} - J_D^{\,2} \tag{46}$$

$$J_{4D} = 2R_D\, J_D \tag{47}$$

where R_D and J_D are obtained using Eqs. (22) and (23). Finally, the real and imaginary parts of the normalized fourth moment are obtained using

$$\mathrm{Re}(M_4) = \langle R_4 \rangle R_{4D} + \langle J_4 \rangle J_{4D} \tag{48}$$

$$\mathrm{Im}(M_4) = \langle J_4 \rangle R_{4D} - \langle R_4 \rangle J_{4D} \quad . \tag{49}$$

2.7 Extrema

For all four antennas, the maximum and minimum observed intensities are obtained. These extremal intensities are normalized by dividing by the mean intensity, because the intensity is measured in arbitrary units. Likewise the maximum and minimum observed phase difference is obtained for each of the six antenna pairs. These extremal phase differences are normalized by subtracting the mean phase difference of the antenna pair, because this mean is an arbitrary offset. Besides being intrinsically interesting, these extrema will take on any greatly erroneous values that appear in the intensities and phase differences. Hence, the extrema reveal erroneous data that are included in all of the other mm-wave statistics described in this report.

2.8 Probability Distribution Functions

We calculate the probability distribution function (PDF) of each of the four intensities. We have control over the range of intensity values included in these PDFs, and foreknowledge of the intensity extrema allows us to efficiently divide the legitimate range of observed values into bins, thereby discarding obviously erroneous data. The PDFs are calculated as histograms by adding unity to the histogram value in a given bin each time the intensity lies within the given bin. These histograms are normalized after the desired amount of data has been included within them. In the same manner we obtain the six phase difference PDFs, one for each antenna pair.

2.9 Fourier Transforms

We calculate the power spectra of each of the four intensities and six phase differences. The computer programs allow us to also calculate cross-

spectra between only two quanties, e.g., between intensities from different antennas, or phase differences from different antenna pairs, or between an intensity and phase difference. By cross-spectra we mean cospectra, quadrature spectra, coherence spectra, or phase spectra of two different quantities.

The fast Fourier transform algorithm is used on 4096-point time series, corresponding to 40.96 s of data. A number of these transforms, nominally 10 of them, are averaged together to increase the statistical reliability. The resulting transforms are combined to produce the aforementioned power and cross-spectra, which are, in turn, each averaged to 36 spectral values in 36 approximately logarithmically spaced frequency bins.

Fourier components of yet lower frequency are obtained by block averaging the time series to 4096 points per data tape (or per time-stationary interval). The data tapes are roughly 2400 s in duration, so averages of roughly 0.6 s suffice. The fast Fourier transforms of these 0.6-s averaged time series are also combined to produce the aforementioned power and cross-spectra and are averaged to 36 logarithmically spaced frequency bins. Finally, these low-frequency spectra are combined with their high-frequency counterparts to form composite spectra having 72 frequency bins. There is adequate spectral overlap between the lowest frequency in the high-frequency part and the highest frequency in the low-frequency part.

2.10 Figures of Merit

Certain redundancies in the mm-wave data make it possible to calculate quantities that would have known values if the measurements were perfect. We call these quantities figures of merit, since their deviations from their ideal values indicate the level of precision in the mm-wave instrumentation.

The first such figure of merit is the ρ type given by

$$\rho^2 \equiv \{[(V_0)^2_{ij} - (V_{180})^2_{ij}]^2 + [(V_{90})^2_{ij} - (V_{270})^2_{ij}]^2\}/I_i\, I_j \,. \qquad (50)$$

There is one ρ-type figure of merit for each of the six antenna pairs. The ρ type is, in effect, the squared modulus of the MCF of the mm-wave instrumentation. Ideally it would have the value unity at each instant, and its

deviations from unity place a limit on the accuracy of measuring the propagation MCF at each antenna separation. We calculate the mean and central variance for these six ρ-type figures of merit.

The second figure of merit is the Σ type given by

$$\sum \equiv [(V_0)^2_{ij} + (V_{90})^2_{ij} + (V_{180})^2_{ij} + (V_{270})^2_{ij}]/(I_i + I_j) \ . \qquad (51)$$

This type, one for each of six antenna pairs, should also be unity at each instant. We calculate the mean and central variance of each of the six Σ's.

The last figure of merit is an obvious one called the "phase" type. If i, j, and k are three distinct antennas such that the k antenna lies between the i and j antennas, then the phase-difference sum $\beta_{ik} + \beta_{kj} - \beta_{ij}$ should ideally be a constant determined by the arbitrary phase-difference offsets of the antenna pairs. Except for these offsets this phase-difference sum would ideally be zero. Because of these offsets, the mean value of this figure of merit is meaningless, but the variance about the mean is a measure of the precision of the phase-difference measurements. This variance is the phase-type figure of merit. The phase-difference variance from each of β_{ik}, β_{kj}, and β_{ij} should be much larger than this figure of merit, otherwise at least one of the phase differences is suspect. There are four such phase-type figures of merit when the antennas are taken three at a time as above, and one when all four antennas are included. The latter is the variance of $\beta_{12} + \beta_{23} + \beta_{34} - \beta_{14}$. We calculate these five figures of merit.

3. QUANTITIES COMPUTED FROM THE NOAA MICROMETEOROLOGICAL DATA

3.1 Introduction

The NOAA micrometeorological data are obtained at two towers, 3.6 m in height, located adjacent to the propagation path at approximately one-third and two-thirds of the distance from the mm-wave receiver to the transmitter. These are designated as stations 1 and 2 respectively, and are shown on Fig. 1. The two optical paths were located 50 m and 65 m east of the mm-wave path. The micrometeorological towers were 80 m east of the mm-wave path, and the

optical rain gauge/disdrometer paths were 90 m east. Each tower has a three-axis sonic anemometer with a platinum resistance-wire thermometer in the center of the sonic array, a nearby Lyman-α hygrometer with another wire thermometer within its gap, a prop-vane anemometer, and a psychrometer for mean temperature and humidity. The wire thermometers and Lyman-α hygrometer were sampled at 100 Hz. The sonic and prop-vane anemometers were sampled at 25 Hz. Beginning with the 0.39-Hz pulse, the psychrometer gives six commutation cycles repeated at the 25-Hz rate. A commutation cycle consists of data from the wet and dry bulbs and two reference values, four quantities in all. The psychrometer then returns toward thermal equilibrium until the next 0.39-Hz pulse calls for data; this minimizes self-heating in the psychrometer due to power dissipation. Station 2 has a Väisälä mean temperature and humidity instrument sampled at 25 Hz, but the Väisälä readings of humidity are judged inferior to those of the psychrometer. Station 2 included an up-looking pyranometer for solar radiation and cloud-shadow-occurrence measurements, and station 1 included a barometer; these were sampled at 25 Hz. A combined optical C_n^2 and optical cross-wind meter was operated on the path from near the mm-wave transmitter to station 1 and another from near the mm-wave receiver to station 2; these optical paths overlap. Optical rain gauges were deployed near both stations and six weighing bucket rain gauges were deployed along the path. At station 1 the optical rain gauge included a disdrometer. The data from these optical instruments were sampled at 0.39 Hz. The reduction of the data from the rain instruments is not discussed in this report.

Additional optical instrumentation was deployed during the fourth experiment session. A 10.6-μm CO_2 laser, for measurement of infrared C_n^2 in clear air and for phase-difference spectra in rain, was operated from near the mm-wave transmitter to inside the mm-wave receiver trailer. A third large-aperture optical C_n^2 and cross-wind meter was operated over the northern two-thirds of the range directly below its existing counterpart. The purpose was to measure vertical shear of the path-averaged optical cross wind. A He-Ne laser scintillometer and LED scintillometer were deployed over the same short path to measure the inner scale of turbulence by its effect on optical scintillation. At station 1 an up-looking photocell was installed to compare cloud cover measurements with those of the up-looking pyranometer at station 2. In addition, another psychrometer was installed at station 2 to determine the instrument's reliability by comparison with its existing counterpart.

Except for the CO_2 laser, these additional instruments were recording data during the second half of the fifth session, as well.

The heights of the instrumentation as well as subjective estimates of the 3σ errors in the heights are as follows: The mm-wave beam and CO_2-laser beam average 3.68 m ± 0.1 m; the Lyman-α gap, horizontal sonic transducers, prop-vane, and platinum wires are at 3.61 m ± 0.05 m; the psychrometer inlets are at 1.91 m ± 0.05 m; the upper-level optical wind and C_n^2 meters and the optical inner-scale meter are at 3.78 m ± 0.1 m; and the lower-level optical wind and C_n^2 meter are 2 m ± 0.02 m below the upper-level meters.

3.2 Conversion to Units

Unlike the mm-wave data, the micrometeorological data must be converted to physical units like degrees Celsius or meters per second. This conversion depends on mean temperature for the sonic anemometers and on mean humidity for the Lyman-α hygrometers. The 0.39-Hz data is converted to units giving a datum from each instrument every 2.56 s. The middle four of the six commutation cycles from the psychrometer are averaged to provide wet- and dry-bulb temperatures at the 0.39-Hz rate. The temperatures from the platinum resistance-wire thermometers and the voltage counts from the Lyman-α hygrometers are averaged over 2.56-s bins to determine their trends. Comparison of these Lyman-α voltage counts averaged over the entire tape with the similarly averaged psychrometer humidity establishes the Lyman-α calibration.

The resistance-wire signals are converted to degrees Celsius and Lyman-α signals are converted to absolute humidity in grams of water vapor per cubic meter, all at their 100-Hz data rate. The prop-vane signals are converted at their 25-Hz data rate to wind speed in meters per second and angle in degrees. This wind angle is zero if the wind is perpendicular to the front of the instrument boom and increases if the vane turns clockwise as viewed from below. The wind components along the sonic axes are converted to meters per second, at their 25-Hz rate. The solar pyranometer output is expressed as a fraction of full sun (1.395 W/m^2) at its 25-Hz rate. The barometer signal is converted to millibars at its 25-Hz rate.

The angle between the horizontal sonic axes is 120° to allow a greater acceptance of wind angle variation. Consequently the measured horizontal

sonic wind components are not orthogonal. Our sonic configuration is shown by Kaimal (1980a; Figs. 2 and 3). Orthogonal components are obtained from the nonorthogonal ones such that the u-component is perpendicular to the instrument boom and is positive when the wind is toward the boom and the v-component is parallel to the boom, and is positive when the wind is blowing right to left of a person facing the boom. If we let V_A and V_B denote the wind components along the "A" and "B" sonic axes as depicted by Kaimal (1980a; Figs. 2 and 3), then u and v are given by

$$u = V_A + V_B \tag{52}$$

$$v = (V_B - V_A)/\sqrt{3} \ . \tag{53}$$

The vertical axes of the sonic anemometer are maintained to within 0.1° of vertical so that the measured vertical wind component, w, is negligibly contaminated by horizontal wind fluctuations. The u, v, and w components then form a right-handed orthogonal triad. Although the boom is rotated into the wind at the beginning of each data run, there remains a slight difference between our notation for u, v, w and the standard micrometeorological notation that the u-component is along the time-averaged direction of the wind (i.e., it is the streamwise component) and that v is the cross-stream component.

Angle encoders at both meteorological towers give the angle of the instrument boom relative to geographic directions. These encoders give angles changing from 0° to 90°, to 180°, to 270° as the boom rotates from facing north to facing east, to facing south, to facing west (N, E, S, W), respectively. (As a result of an error, these encoder angles are for directions W, N, E, S for the first two data tapes of the third experiment session.) We define the geographic wind angle as the encoder angle minus the prop-vane angle. As mentioned before, the vane angle is relative to the boom; it increases clockwise when one looks up at the boom from below, and is zero for wind blowing into the face of the boom. The geographic wind angle is then 0°, 90°, 180°, and 270° for wind blowing from the N, E, S, and W, respectively. (Except for the first two data tapes of the third experiment session when these angles are for wind from the W, N, E, and S, respectively.) The optical cross wind telemetered from station 1 is obtained over the southern two-thirds of the mm-wave range and is positive for wind from the east. The optical cross wind telemetered from station 2 is obtained over the northern two thirds of the range and is positive for wind from the west.

3.3 Averages, Variances, and Cross-Correlations

Table 3 lists the averages performed in each computation. An average is denoted by the angle brackets. The symbols for the quantities are as follows: q is the Lyman-α humidity in grams per cubic meter; T_L is the temperature in Celsius from the resistance wire within the Lyman-α gap; T_S is the temperature in Celsius from the resistance wire within the sonic anemometer; u, v, w are the orthogonalized sonic anemometer wind components in meters per second as discussed in Sec. 3.2; V and θ are the prop-vane wind speed in meters per second and angle in degrees, respectively; S is the pyranometer solar flux.

Table 3.--Kinds of averages performed on the NOAA micrometeorological data

Averages	$\langle q \rangle$, $\langle T_L \rangle$, $\langle T_S \rangle$, $\langle u \rangle$, $\langle v \rangle$, $\langle w \rangle$, $\langle V \rangle$, $\langle \theta \rangle$, $\langle \sqrt{u^2 + v^2} \rangle$, $\langle S \rangle$
Mean squares	$\langle q^2 \rangle$, $\langle T_L{}^2 \rangle$, $\langle T_S{}^2 \rangle$, $\langle u^2 \rangle$, $\langle v^2 \rangle$, $\langle w^2 \rangle$, $\langle V^2 \rangle$, $\langle \theta^2 \rangle$, $\langle u^2 + v^2 \rangle$, $\langle S^2 \rangle$
Cross-correlations	$\langle u\ w \rangle$, $\langle v\ w \rangle$, $\langle u\ v \rangle$, $\langle q\ w \rangle$, $\langle T_L\ w \rangle$, $\langle T_S\ w \rangle$, $\langle q\ T_L \rangle$, $\langle q\ T_S \rangle$, $\langle T_L\ T_S \rangle$, $\langle \sqrt{u^2 + v^2}\ w \rangle$

Note: See text for an explanation of the symbols.

The averages listed in Table 3 are obtained for both micrometeorological stations. In the case of cross products like $\langle T_S\ w \rangle$, which have a 100-Hz quantity, T_S, multiplied by a 25-Hz quantity, w, we average four consecutive values of the 100-Hz quantity before performing the product and including the term in the summation.

The mean squares and cross-correlations given in Table 3 are not of interest in themselves. After the averaging is completed the mean squares are converted to variances taken about the mean (centralized variances) and the cross-correlations are likewise converted. The following equations give the

desired central moment on the left side and the required calculation on the right side. For the variances, where Q may be w, u, v, V, T_S, T_L, or q, we use

$$\langle (Q - \langle Q \rangle)^2 \rangle = \langle Q^2 \rangle - \langle Q \rangle^2 \ . \tag{54}$$

For the centralized cross-correlations, where the pair Q_1, Q_2 may be u,w or v,w or u,v or q,w or T_L,w or T_S,w or T_L,q, we use

$$\langle (Q_1 - \langle Q_1 \rangle)(Q_2 - \langle Q_2 \rangle) \rangle = \langle Q_1 \ Q_2 \rangle - \langle Q_1 \rangle \langle Q_2 \rangle \ . \tag{55}$$

We subtract the mean of quantities like w, which should have a zero mean value, because instrumental offsets cause the measured values to have nonzero means, and these offsets must be subtracted.

3.4 Turbulence Fluxes

All of the quantities discussed in this section are obtained from averages previously performed. The correlations discussed in the previous section form the basis for the calculation of the fluxes.

The quantities $\langle (T_S - \langle T_S \rangle)(w - \langle w \rangle) \rangle$ and $\langle (q - \langle q \rangle)(w - \langle w \rangle) \rangle$ are the vertical fluxes of temperature and humidity, respectively. Temperature flux can be converted to heat flux by multiplying by the constant-pressure heat capacity of air, and humidity flux can be converted to latent heat flux by multiplying by the latent heat of vaporization. The above temperature flux is obtained by correlating the fluctuating temperature from the resistance-wire thermometer within the sonic array with the fluctuating vertical velocity from the sonic anemometer. The Lyman-α hygrometer is spatially separated from the sonic array so that it does not disturb the turbulent wind field at the array. The spatial separation slightly reduces the humidity flux from its true value. However, we also calculate the temperature flux using the resistance wire within the Lyman-α gap from the cross-correlation $\langle T_L \ w \rangle$. The ratio of the two temperature fluxes,

$$\langle (T_L - \langle T_L \rangle)(w - \langle w \rangle) \rangle / \langle (T_S - \langle T_S \rangle)(w - \langle w \rangle) \rangle \ , \tag{56}$$

is a correction factor for this spatial separation. Because of the high correlation and/or anticorrelation between temperature and humidity fluc-

tuations, the humidity flux can be multiplied by this ratio to correct it for the spatial separation.

To obtain the vertical flux of horizontal momentum we must cross-correlate fluctuating vertical wind speed with the fluctuating horizontal wind component along the time-averaged wind direction (the streamwise component). Given the mean wind angle $\langle\theta\rangle$ from either the vane or sonic anemometer, the streamwise component u_θ and cross-stream component v_θ are given in terms of the u and v components by

$$u_\theta = u \cos\langle\theta\rangle + v \sin\langle\theta\rangle \tag{57}$$

$$v_\theta = -u \sin\langle\theta\rangle + v \cos\langle\theta\rangle \ . \tag{58}$$

Letting primes denote zero-mean fluctuations, e.g., $u_\theta' = u_\theta - \langle u_\theta\rangle$ and $v' = v - \langle v\rangle$, then we have

$$u_\theta' = u' \cos\langle\theta\rangle + v' \sin\langle\theta\rangle \tag{59}$$

$$v_\theta' = -u' \sin\langle\theta\rangle + v' \cos\langle\theta\rangle \ . \tag{60}$$

The vertical momentum flux is given by multiplying the quantity

$$\langle u_\theta' \, w'\rangle = \langle u' \, w'\rangle \cos\langle\theta\rangle + \langle v' \, w'\rangle \sin\langle\theta\rangle \tag{61}$$

by the mass density of the air. Calculation of the quantities

$$\langle u' \, w'\rangle = \langle u \, w\rangle - \langle u\rangle\langle w\rangle \tag{62}$$

and

$$\langle v' \, w'\rangle = \langle v \, w\rangle - \langle v\rangle\langle w\rangle \tag{63}$$

has already been discussed in the previous section. The vertical flux of cross-stream momentum

$$\langle v_\theta' \, w'\rangle = - \langle u' \, w'\rangle \sin\langle\theta\rangle + \langle v' \, w'\rangle \cos\langle\theta\rangle \ , \tag{64}$$

and the horizontal flux of momentum obtained from

$$\langle u_\theta' \, v_\theta' \rangle = 1/2(\langle v'^2 \rangle - \langle u'^2 \rangle) \sin(2\langle\theta\rangle) + \langle u' \, v' \rangle \cos(2\langle\theta\rangle) \qquad (65)$$

should both be zero for a horizontally homogeneous surface layer, but they are computed anyway. In addition, for station 2 we calculate the speed flux given by

$$\left\langle \left(\sqrt{u^2 + v^2} - \langle \sqrt{u^2 + v^2} \rangle \right) (w - \langle w \rangle) \right\rangle = \langle \sqrt{u^2 + v^2} \, w \rangle - \langle \sqrt{u^2 + v^2} \rangle \langle w \rangle \, . \qquad (66)$$

We can calculate the momentum flux using (61) in a variety of ways depending on how we choose $\langle\theta\rangle$. We could, for instance, take $\langle\theta\rangle$ to be the average of the vane angles. The conventional method is to set the average cross-stream component to zero, i.e., $\langle v_\theta \rangle = 0$, so from (58) $\langle\theta\rangle = \arctan(\langle v \rangle / \langle u \rangle)$ as given by Kaimal (1980a). However, this $\langle\theta\rangle$ is sensitive to the poorly-known offset voltages of the sonic anemometer. On the other hand, we can assume a horizontally homogeneous surface layer and set $\langle v_\theta' \, w' \rangle = 0$ in (64) to define $\langle\theta\rangle$; this definition of $\langle\theta\rangle$ is independent of sonic offset voltages. Using this latter $\langle\theta\rangle$, (61) gives for the momentum flux

$$\langle u_\theta' \, w' \rangle = \sqrt{\langle u' \, w' \rangle^2 + \langle v' \, w' \rangle^2} \, .$$

This result is independent of sonic offset voltages, but depends on horizontal homogeneity. We calculate this latter momentum flux, but we also use the mean vane angle to calculate the expressions in (61), (64), and (65).

3.5 Spatial Structure Parameters

The spatial separation of the two resistance-wire thermometers and of the Lyman-α hygrometer and the resistance wire within the sonic anemometer enable us to calculate temperature structure parameters and temperature-humidity cross-structure parameters. The temperature structure parameter is given by

$$C_T^2 = \langle (T_S' - T_L')^2 \rangle / r_{SL}^{2/3} \qquad (67)$$

$$= (\langle T_S^2 \rangle - \langle T_S \rangle^2 + \langle T_L^2 \rangle - \langle T_L \rangle^2 - 2\langle T_S \, T_L \rangle + 2\langle T_S \rangle \langle T_L \rangle) / r_{SL}^{2/3} \qquad (68)$$

where primes denote zero-mean fluctuations and r_{SL} is the distance between the resistance-wires in the sonic anemometer and the Lyman-α gap. The second formula (68) shows that this structure parameter can be calculated from quantities already discussed in Sec. 3.3.

If we had additional Lyman-α hygrometers positioned within the sonic anemometer yielding fluctuating humidities q_S', then we could calculate the temperature-humidity cross-structure parameter defined by

$$C_{Tq} = \langle (T_S' - T_L')(q_S' - q') \rangle / r_{SL}^{2/3} \quad . \tag{69}$$

However, if we assume that this hypothetical hygrometer would give $\langle T_S' \, q_S' \rangle = \langle T_L' \, q' \rangle$ and $\langle T_S' \, q' \rangle = \langle T_L' \, q_S' \rangle$ (the latter requires horizontal isotropy), then we have

$$C_{Tq} = 2(\langle T_L' \, q' \rangle - \langle T_S' \, q' \rangle)/r_{SL}^{2/3} \tag{70}$$

$$= 2(\langle T_L \, q \rangle - \langle T_L \rangle \langle q \rangle - \langle T_S \, q \rangle + \langle T_S \rangle \langle q \rangle)/r_{SL}^{2/3} \quad , \tag{71}$$

where (71) shows that the calculation obtains from quantities already discussed in Sec. 3.3.

3.6 Time-Lagged Structure Parameters

The time-lagged structure parameters of temperature, C_T^2, humidity, C_Q^2, C_q^2, and the temperature-humidity cross-structure parameter, C_{Tq}, are defined by

$$C_{T_S}^2 = \langle [T_S(t) - T_S(t + \tau)]^2 \rangle / (\langle V \rangle \tau)^{2/3} \quad , \tag{72}$$

$$C_{T_L}^2 = \langle [T_L(t) - T_L(t + \tau)]^2 \rangle / (\langle V \rangle \tau)^{2/3} \quad , \tag{73}$$

$$C_q^2 = \langle [q(t) - q(t + \tau)]^2 \rangle / (\langle V \rangle \tau)^{2/3} \quad , \tag{74}$$

$$C_{T_L q} = \langle [T_L(t) - T_L(t + \tau)][q(t) - q(t + \tau)] \rangle / (\langle V \rangle \tau)^{2/3} \quad , \tag{75}$$

where t is time, τ is time lag, and $\langle V \rangle$ is the average wind speed. The data are digitized at 100 Hz, so τ must be a multiple of 0.01 s. Let the height above ground be denoted by Z, then Z/5 should be in the inertial range of

sizes. We define a dimensionless factor by

$$F \equiv (Z/5)(100 \text{ samples/s})/\langle V \rangle \ . \tag{76}$$

We then define three integers $J_1 = F$, $J_2 = F/2$, and $J_3 = F/4$, where the integers are rounded up from the real numbers. These integers are the number of 0.01-s data samples to skip to calculate the above four structure parameters for both stations at three values of time lag. The time lags used are thus $\tau_1 = J_1(0.01 \text{ s})$, $\tau_2 = J_2(0.01 \text{ s})$, and $\tau_3 = J_3(0.01 \text{ s})$; these correspond approximately to spatial lags of Z/5, Z/10, and Z/20. The integers and lags can be different at the two stations because $\langle V \rangle$ can differ between the stations.

Of course, the time-lagged structure parameters and cross-structure parameters can also be obtained from the spectral level of the appropriate power spectra and cospectra, which are discussed in Sec. 5.9.

3.7 Extrema

We obtain the minimum and maximum observed values of several quantities for each averaging period. These quantities are the wind speed and wind angle from the prop-vane anemometer and the solar flux from the pyranometer.

3.8 Probability Distribution Functions

The probability distribution functions (PDFs) are calculated for the pyranometer solar flux and the wind angles from the two prop-vane anemometers. The joint probability distribution functions (JPDFs) of Lyman-α humidity and its associated resistance-wire temperature is calculated for both stations. The PDFs of the fluctuating humidity or temperature can be obtained by summing the JPDF over all temperature or humidity bins, respectively. These PDFs obtained from JPDFs are sometimes called marginal PDFs. Since for clear air the fluctuations of real and imaginary parts of the refractive index depend almost entirely on only temperature and humidity fluctuations, we can obtain the JPDF of these real and imaginary parts from the temperature-humidity JPDF.

Of course, the marginal PDFs of refraction and absorption can be obtained from this latter JPDF as well.

The method of calculating these PDFs and JPDFs as histograms using foreknowledge of the extrema to divide efficiently the data into bins is the same as was discussed for the mm-wave PDFs in Sec. 2.8.

3.9 Fourier Transforms

We calculate the power spectra of the fluctuating temperature and humidity from the resistance-wires and the Lyman-α hygrometer, as well as the temperature-humidity cospectra and quadrature spectra from these instruments. We also calculate the power spectra of all three orthogonalized components of the fluctuating wind from the sonic anemometers, as well as the cospectra and quadrature spectra of these components taken in pairs. The cospectra and quadrature spectra are calculated for temperature and vertical velocity, and for humidity and vertical velocity.

The fast Fourier transform (FFT) algorithm is used on 4096-point time series. This corresponds to 40.96 s of data if only 100-Hz quantities are involved or 163.84 s of data if at least one quantity is of the 25-Hz sampling rate. A number of these FFTs are averaged together, nominally 10 of them, to increase the statistical reliability. As with the mm-wave Fourier transforms, the FFTs are combined to produce power spectra and cross-spectra that are similarly averaged into 29 logarithmically spaced frequency bins.

3.10 Refraction and Absorption Structure Parameters

The zero-mean fluctuations in the real and imaginary parts of the refractive index, denoted n_R' and n_I', respectively, are related to those of temperature and humidity by

$$n_R' = \frac{A_T}{\langle T \rangle} T_L' + \frac{A_q}{\langle q \rangle} q' \tag{77}$$

$$n_I' = \frac{B_T}{\langle T \rangle} T_L' + \frac{B_q}{\langle q \rangle} q' \tag{78}$$

where $\langle T \rangle$ is the mean Kelvin temperature, the effects of pressure fluctuations are neglected, and these equations are valid for fluctuations much smaller than the means. The dimensionless sensitivity coefficients A_T, A_q, B_T, and B_q depend on mean temperature, humidity, pressure, and the electromagnetic wave length; they are calculated from the radio-frequency refractive-index equation, as well as the sum of dispersion and absorption contributions from water vapor and oxygen resonances, oxygen and nitrogen nonresonant absorption, and the water vapor anomalous absorption. The computer programs for this calculation are not discussed here.

Equations (77) and (78) provide statistics of refraction and absorption from those of temperature and humidity. For instance, the refractive-index structure parameters are given by

$$C_{n_R}^2 = \frac{A_T^2}{\langle T \rangle^2} C_{T_L}^2 + \frac{A_q^2}{\langle q \rangle^2} C_q^2 + \frac{2A_T A_q}{\langle T \rangle \langle q \rangle} C_{T_L q} \tag{79}$$

$$C_{n_I}^2 = \frac{B_T^2}{\langle T \rangle^2} C_{T_L}^2 + \frac{B_q^2}{\langle q \rangle^2} C_q^2 + \frac{2B_T B_q}{\langle T \rangle \langle q \rangle} C_{T_L q} \tag{80}$$

$$C_{n_R n_I} = \frac{A_T B_T}{\langle T \rangle^2} C_{T_L}^2 + \frac{A_q B_q}{\langle q \rangle^2} C_q^2 + \frac{A_T B_q + A_q B_T}{\langle T \rangle \langle q \rangle} C_{T_L q} \quad . \tag{81}$$

If these structure parameters are replaced by their corresponding power spectra and cospectra, then these equations give the power spectra and cospectra of refraction and absorption in terms of those of temperature and humidity. Likewise, by analogous replacement, these equations express the variances and cross-correlations of refraction and absorption in terms of those of temperature and humidity.

Clearly, all the relevant statistics of refraction and absorption fluctuations can be obtained from the already-calculated micrometeorological statistics once the sensitivity coefficients are known. In particular, the linear relationships (77) and (78) make it easy to calculate the joint probability distribution function of n_R' and n_I' from that of fluctuating temperature and humidity.

4. PROBLEMS WITHIN THE DATA

4.1 Introduction

The greatest fraction of personnel time expended on the data processing software has been used to fix problems in the data. The discovery and diagnosis of these problems has been challenging and time consuming. During the July 1983 session, the data aquisition system dropped occasional bytes, dropped data frames of 0.01-s duration as well as entire blocks of data of 0.16-s duration, and wrote parity errors on the data tapes. The aquisition system was modified for subsequent sessions. The mm-wave data contain the expected data dropouts during periods of phase-lock loss, but they also contain occasional spikes, step changes in signal gain, harmonic noise due to vibration of the steel I-beam holding the receivers, and other noise of unknown origin. During the first session, the intensity at antenna 4 is incorrect. The micrometeorological data had several instrument failures during that session. The Lyman-α hygrometer at station 1 was not working; one of the optical wind and C_n^2 meters was not working; the resistance-wire thermometer signals exhibited cold spikes and hot spikes that are characteristic of contamination of the wire by hydroscopic particles; and the sonic anemometer signals contained numerous spikes (one per several seconds per channel). Most of these problems have been solved by clever but time-consuming software development.

4.2 Cures for Data Aquisition Errors

A data frame is the digitized data from all instruments in each one-hundredth of a second. The first byte in each frame is synchronization (sync) information. It was found that some of these sync bytes are missing from the data tape. Since the sync bytes should arrive with every frame, it was possible to insert the missing byte when the data tapes were rewritten for our data processing computer.

Entire data frames were found to be missing with no gap in frame sync bytes. The first experiment session had a 10-Hz clock written to tape, so precise frame loss detection is impossible. The 25-Hz data are written to tape by repeating the same value four times for each 25-Hz channel; missing

data frames manifest themselves by fewer than four repetitions of 25-Hz data. A special flag is set to unity in the first data frame of this 25-Hz repetition and set to zero for the last three frames in the repetition. Using this special flag it is possible to identify how many frames are missing, assuming not more than three frames were lost. We then replace the missing frame or frames by duplicating the frame preceding the occurrence of lost frames and setting the special flags when necessary. This restores the integrity of the 25-Hz and 0.39-Hz data and the temporal continuity of the data. Beginning with tape 12 of session 2 through session 5, the lost frame detection is much easier since the 100-Hz clock channel shows each frame that is out of sequence. Changes in the data aquisition system for runs after the tape 12 of session 2 have apparently stopped the frame-loss problem.

The data acquisition system writes data to magnetic tape one block at a time; a block consists of 16 frames, i.e., 0.16 s of data. During session 1, if the read-after-write check failed, then the block was rewritten on tape. The time consumed in the rewrite caused the next block of data to be lost. Thus entire data blocks are missing from session 1 data tapes. The rewrite was disabled for subsequent experiment sessions to avoid this block-loss mechanism. We cannot recreate lost blocks. However, their approximate positions on the data tapes can be identified using the system time (accurate to 0.1 s in session 1 and 0.01 s in subsequent sessions) that is written into each frame. The positions of these lost blocks are written to the "pedigree" disk file so that these data gaps can be avoided during Fourier transformation. So far, no block losses have been found following changes in the data acquisition system that were implemented just before tape 12 of session 2.

The data aquisition system wrote parity errors onto the data tapes. Roughly one-half of all data tapes contain a parity error. By turning off the error processing, we can read the data tape in an unsafe mode. To date this has been tried on only two data tapes. The problem of the parity errors exists in all five experiment sessions.

4.3 Cures for Millimeter-Wave Data Problems

All 28 mm-wave channels require a correction as a result of nonlinearity of the detectors. (The crystal detectors in the signal combiner are not

perfect-square-law detectors in the radio-frequency power regime used.) The extent of nonlinearity was measured for each of the 28 channels and fitted by a polynomial. In the data analysis each datum for each mm-wave channel and for every 0.01 s was corrected by evaluating a fourth-order polynomial (roughly 7 million polynomial evaluations per data tape). One set of polynomial coefficients is used for session 1, another set for session 2 through tape 10 of session 3, and yet another set thereafter. This is necessary because different RF input power was used.

The intensity at antenna 4, I_4, was not measured during session 1 because of a hard-wiring error. Fortunately, the redundancy in the mm-wave data allows us to calculate I_4 as follows. If ρ^2 in Eq. (50) is obtained from an antenna pair including antenna 4, then setting $\rho^2 = 1$ allows us to calculate I_4 from the other channels. Likewise setting $\Sigma = 1$ in Eq. (51) gives the same result. We wrote a separate computer program to evaluate these methods of synthesizing an intensity. The program compared the normalized variance of the three intensities I_1, I_2, and I_3 with their synthesized values from every relevant antenna pair as well as averages of the synthetic intensities over every combination of such antenna pairs. We determined that setting $\Sigma = 1$ produced better results than setting $\rho^2 = 1$ and that averaging the synthesized intensities improved the reliability. For the test case the difference between normalized variances from measured and synthesized intensities ranged from 13.5% to a few tenths of a percent for the $\Sigma = 1$ method, and the normalized variance from the synthesized I_4 was 17% smaller than that from I_1, I_2, and I_3. There is no guarantee that such good results will be obtained from all of session 1 data tapes. At present we use the $\Sigma = 1$ method to synthesize three values of I_4 from the three antenna pairs containing antenna 4 and average these three I_4 values together to produce I_4 for each 0.01-s data frame.

The mm-wave data contain trends that have no correspondence to meteorological trends, nor do the trends in one mm-wave channel appear related to trends in other channels. These trends are apparently caused by drift in receiver gains. Consequently we filter the four intensities and six phase differences using single-pole digital low-pass filters having a roughly 125-s time constant. The filter value is subtracted from the phase differences but divided into the intensities. We retain the unfiltered mean value of the four

intensities. (The figures of merit are obtained from unfiltered data.) However, this filtering requires that we discard about 5 min of data from the beginning of each data tape to initialize the filter.

The mm-wave data contain the expected periods of phase-lock loss. These are of variable duration but typically less than 20 s. There are a variety of types of these data dropouts. The mildest type appears to have intact data, but the intensity drops to half its usual value. The most severe type reduces all mm-wave channels to noise. We detect these phase-lock-loss periods visually using computer-generated microfilm stripcharts. We note the beginning and ending times of each such loss on these stripcharts and enter them in the parameters file for use in subsequent processing. Thus we can exclude the phase-lock losses from subsequent processing. This greatly complicates our programming because we must archive the beginning and ending times, determine what averaging intervals contain such a loss, determine whether or not the loss extends across the boundary of an averaging interval, keep account of the number of samples averaged in each interval, avoid the intervals in the high-frequency FFT, and replace the data with fake values for both the digital filtering and low-frequency FFT.

The mm-wave data also occasionally contain spurious spikes of unknown origin in one or several channels. Sometimes these spikes come in groups of many randomly spaced spikes. We identify these spikes from the microfilm stripcharts and note the time interval containing the spike. We then treat the interval as a phase-lock loss and exclude all mm-wave data in this interval from the data processing. This creates the same complications for our processing as do the phase-lock loss periods. A sophisticated "despiker" algorithm could be used to salvage more data.

On some data tapes, one or more mm-wave channels will exhibit a step change occurring in a time less than 0.01 s. Later, other such step changes may occur, either in the same direction or the opposite. At present we are not processing the data tapes containing this type of error.

Most of the mm-wave data contain noise. One source of noise is harmonic vibration of the steel I-beam that supports the mm-wave receivers. This noise tends to come and go and may be generated by wind gusts stressing the receiver semitrailer, which transmits the stress to the ground and then to the I-beam

supports. The differential motion of parts of the I-beam toward and away from the transmitter causes an artificial phase difference. The most common and largest amplitude of this type of noise is at roughly 5 Hz. Higher frequencies have also been observed. A form of noise in the phase differences that does not seem to be caused by I-beam vibration is a roughly 24-Hz oscillation modulated by a roughly 3-Hz oscillation giving a popcorn-on-a-string effect. This noise can cover entire data runs and persist from one run to another. Even higher frequency noise sometimes appears in intensities as well as in phase differences. The mm-wave Fourier transform is used to identify the frequencies and bandwidths of these noise types. Time-domain convolution filters are used on the time series of the four intensities and six phase differences. Low-pass filtering is especially effective on the phase differences. For any one of the 10 time series there may be one, none, or several such filters acting on different frequencies with different bandwidths.

4.4 Cures for Micrometeorological Data Problems

For those instruments that are not functioning properly during a data run or session, we simply process their signal anyway. It is then necessary to ignore the reduced data from these instruments when the averaged results are interpreted. In session 1, this is the case with the Lyman-α hygrometer at station 1 as well as with one of the optical wind and C_n^2 meters. The wet bulb in the psychrometer at station 1 is dry over most of session 1.

The platinum resistance-wire thermometers have numerous cold and hot spikes that have the same signature as those observed in the marine surface layer by Schmitt et al. (1978). These are particularly evident in session 1. In the marine case the wires rapidly become contaminated by salt spray; the hydroscopic nature of the sodium cloride causes random evaporative cooling and condensative heating of the wire because the fluctuating humidity continually drives the adhering salt-water solution away from equilibrium. We hypothesize that our signals are contaminated by some hydroscopic particles adhering to our wires. This effect has never before been observed in over-land data. We cannot test this hypothesis because the experiment session ended before the effect was observed. However, considering only session 1 data, it is a plausible hypothesis because of the high relative humidities (above 85%) and the close similarity of the signal to that observed for salt-spray-

contaminated data. We do not know the source of hydroscopic aerosol, but we speculate that it may be related to fertilization of the soil or herbicide spraying or washing of the wires in a weak solution of baking soda during manufacture. Field tests were conducted during session 4 under high humidity conditions, but the effect did not reappear during the test. In session 2 the electronics were tested as a source of these spikes but found not to be at fault. However, the hot and cold spikes were present in data taken during session 2.

The cold- and hot-spike phenomenon has serious consequences for our statistics. As shown by Schmitt et al. (1978), temperature structure parameters and heat fluxes are seriously overestimated in marine surface-layer data. The effects are spectrally broad so that simple digital filtering will not help. In effect, the resistance-wire signal is responding to a combination of the air temperature variation and the time-derivative of the humidity. In the future we will examine whether or not this effect can be parameterized. If so, then it may be possible to use the temporal derivative of humidity from the Lyman-α hygrometer to correct the temperature signal from the resistance wire that is within the Lyman-α gap. Such a correction will be a run-by-run, trial-and-error approach based on the parameterization having variable parameters. In the mean time we calculate contaminated statistics with a cautionary note as to their accuracy.

There are occasional spikes in one or more of the 100-Hz channels that are of electronic origin unrelated to the above-mentioned signal contamination. We observe these on computer-generated microfilm stripcharts and note times immediately preceding and following these spikes. The data processing then skips all of the given station's 100-Hz and 25-Hz data within the interval defined by these noted times. This is the same procedure as was used for the mm-wave processing, and it imposes the same complications on the processing software.

During experiment sessions 1 and 2, all three axes of both sonic anemometers produced numerous spikes that were triggered by power-line noise and sonic electronics that were excessively sensitive to such effects. These spikes occurred at a rate of roughly one per several seconds per sonic axis. Their occurrences and strengths are random and sometimes coincident in several axes. Fortunately, in almost all cases a spike consists of only one erroneous

datum. A despiking subroutine has been written that recognizes the spikes by the sudden change of signal, first in one direction then in the other, that exceeds a threshold set at 1 standard deviation of the time series. This threshold was chosen by trial and error. If the standard deviation of the despiked data differs significantly from that of the original data, then the despiking is repeated. This procedure removes the spikes and has very little effect on the data. Of many thousands of spikes removed, only four double-datum spikes of relatively low amplitude remain in the data of session 1. Although the despiking subroutine can remove double-datum spikes by first averaging the data in temporally adjacent pairs, these few remaining spikes are judged to be too insignificant for this procedure. Moreover, the remaining spikes can be excluded from the data processing by previously discussed methods. The problem of the sonic spikes is thus solved.

The existence of sonics spikes prohibited nulling of the sonic electronics in the field for sessions 1 and 2. Normally this null calibration produces zero signal from the sonics when the axes are covered so that no wind is present. Thus all the sonic axes have offset wind readings amounting to as much as ±0.6 m/s per axis. This is not a problem for the vertical axes, because we subtract $\langle w \rangle$ for all of our calculated statistics involving w, and the vertical axes were maintained within 0.1° of vertical, so horizontal wind fluctuations negligibly contaminate the measured vertical fluctuations. The offset is serious for the horizontal axes. Fortunately there is an adjacent prop-vane anemometer with which to compare wind readings, so the offset can be measured.

Take the sonic A component as an example. The true sonic A component, A_t, is given in terms of the measured and despiked A component, A_m, and the offset O_A by

$$A_t = (A_m - O_A)\, K^{-1} , \tag{82}$$

where K is the wake correction factor given by Kaimal (1980b). The inverse of K appears on the right side of (82) because Kaimal defines K as the ratio of measured to true sonic components. Also, K is a function of the angle between the wind vector and the sonic arm. We would like to calculate the A component from the prop-vane anemometer, A_p, and require that $\langle A_p \rangle = \langle A_t \rangle$. However, we do not a priori know the sonic-derived angle between the wind vector and the

sonic arm because of the offset. Thus we cannot make the wake correction to A_m or eliminate data when the wind is outside of the ±45° acceptance angle. Instead, we average (82), eliminating data when the vane angle is outside the ±45° acceptance angle, and similarly average A_p. Replacing $\langle A_t \rangle$ by $\langle A_p \rangle$, we have from (82),

$$\langle A_p \rangle = \langle A_m \, K^{-1} \rangle - O_A \langle K^{-1} \rangle \ , \tag{83}$$

wherein K is calculated using the vane angle to infer the angle between the wind vector and sonic arm. The offset is obtained from (83):

$$O_A = (\langle A_m \, K^{-1} \rangle - \langle A_p \rangle)/\langle K^{-1} \rangle \ . \tag{84}$$

To obtain O_A, we thus calculate the three averaged quantities in (84) using the vane angle for both K and the ±45° acceptance-angle criterion. Equation (84) is not exact, but it need only be a good statistical approximation. We have had excellent results using (84). That is, using (84) for O_A in (82) and the analogous calculation for the B sonic component, we then obtain the angles between the wind vector and sonic arms from the sonic data. We use this sonic-derived angle to determine both K and the ±45° acceptance-angle criterion. The resulting A_t gives $\langle A_t \rangle = \langle A_p \rangle$ to excellent approximation. The simpler method of setting K = 1 in (84) and not eliminating any data based on the acceptance-angle criterion gives poorer results.

5. OVERVIEW OF THE DATA PROCESSING SOFTWARE

5.1 Introduction

As mentioned in Sec. 1, the data processing software is designed to produce answer files that do not limit interpretation of the data, to cure aforementioned problems within the data, and to produce graphic visualization of data validity at several steps in the processing. The first step is to make a copy of each data tape using a PDP-11/70 computer. This protects the original data tape from being destroyed or altered in subsequent use. The remainder of processing is done on a Cyber 750 computer. This section describes the software used on the Cyber 750. Figure 2 is a flow chart of the computer programs and magnetic tape and disk storage.

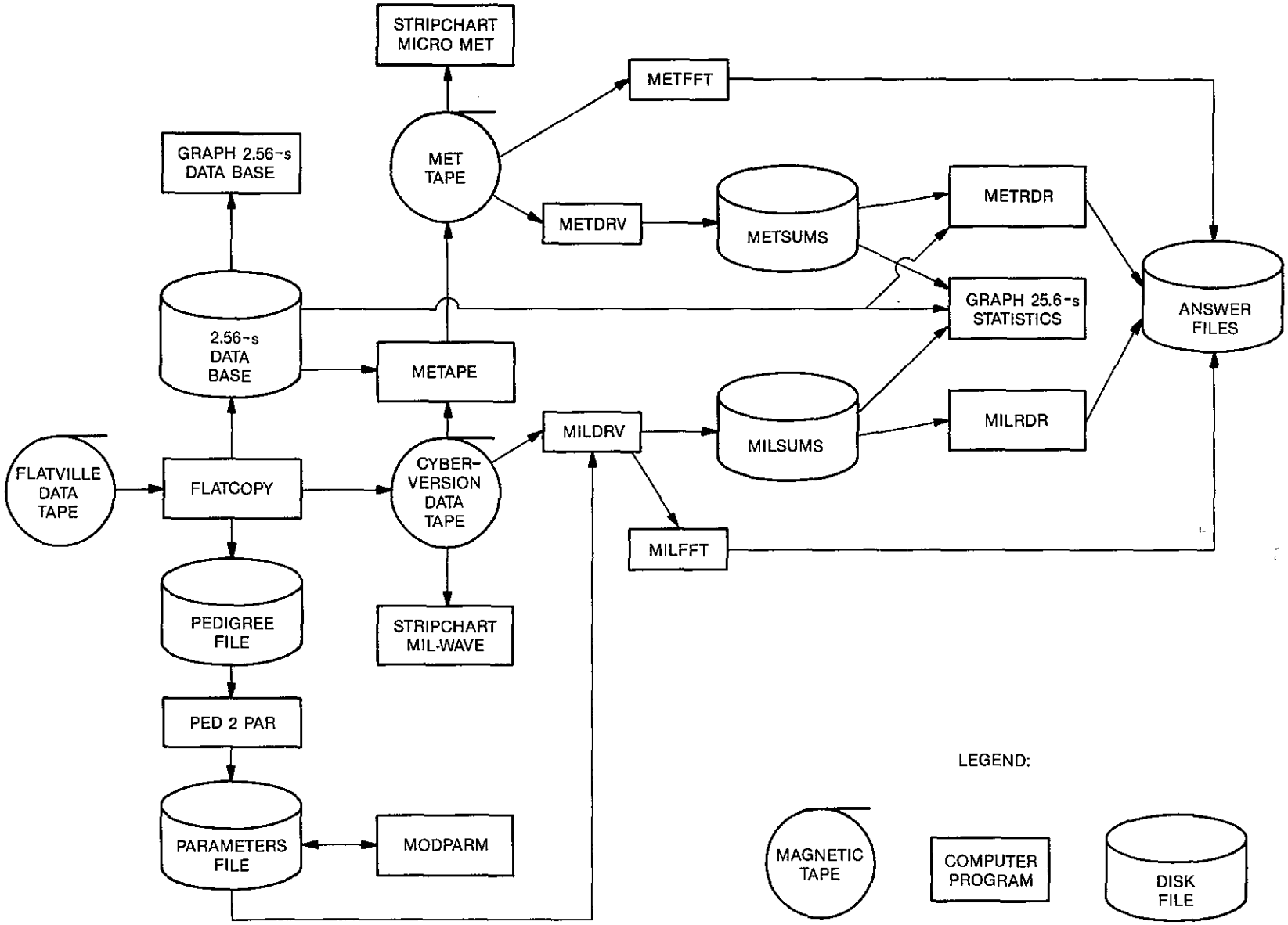

Figure 2.--Overview of the data processing software.

5.2 FLATCOPY

The first step in Cyber processing is program FLATCOPY shown on Fig. 2. FLATCOPY reads the 1600-bpi Flatville data tape (the copy made on the PDP-11/70), which has 1024 words per block, converts the data to 60-bit words, and writes the results to the 6250-bpi Cyber-version data tape. It is this translated Cyber version that is efficiently read by the Cyber 750 in subsequent processing. By using 6250 bpi and blocks of 4096 words, a single Cyber-version magnetic tape contains almost all of the data from a Flatville data tape; the remaining data, if any, are discarded.

FLATCOPY also replaces the missing sync bytes and data frames, and locates the missing data blocks. The times of occurrence of skipped data frames and of the approximate first and last times bracketing a block loss are written to a disk file known as the pedigree file; this file is shown on Fig. 2. The pedigree-file information is used in subsequent processing.

FLATCOPY also extracts the 0.39 Hz data and averages the Lyman-α voltage counts as well as platinum resistance-wire temperatures into 2.56-s bins. This information is written to a 2.56-s meteorological data base disk file that is used in subsequent processing. This 2.56-s data base disk file is shown on Fig. 2. The following processing of 0.39-Hz data occurs in FLATCOPY. The optical disdrometer data are converted to drop-size distribution and the rain rate in volts; both are recorded every 2.56 s in the disk file. The Väisälä signals are converted to temperature in Celsius and to both relative humidity and absolute humidity, and recorded every 2.56 s in the disk file. The barometer signal is converted to millibars and likewise sent to the 2.56-s disk file. Every 2.56 s, the psychrometer wet- and dry-bulb temperatures are derived in Celsius; absolute humidity is also obtained, and all three are written to disk. Psychrometer data are rejected if a frame replacement occurred during the psychrometer commutation cycle; otherwise, spurious results would be obtained. The optical cross-wind and C_n^2 meter data are obtained every 2.56 s in units of meters per second and $m^{-2/3}$ and likewise written to the disk file. The angle encoder's angles in degrees as well as the vane angles averaged in 2.56-s bins and prop-vane wind speeds averaged in 2.56-s bins are written to the 2.56-s data base.

For the fourth and fifth experiment sessions additional optical instrumentation was deployed and their outputs are converted to engineering units and

written to the 2.56-s data base. One such instrument was an additional optical cross-wind and C_n^2 meter at a lower height directly beneath the station 2 optical cross-wind and C_n^2 meter. The purpose is to measure shear in the optical cross wind. Another pair of optical sensors, a He-Ne laser scintillometer with a large-aperture, modulated LED scintillometer, are used together to obtain the inner scale of turbulence. The nominal C_n^2 values obtained from both scintillometers using inertial-range formulas for their log-amplitude variances are recorded in the 2.56-s data base as are the resulting optical inner-scale values.

For rain, fog, snow, or blowing snow the 2.56-s data base contains all of the NOAA meteorological information. An exception is experiment session 5, during which the Lyman-α hygrometer and its resistance-wire thermometer are shielded from precipitation in an attempt to measure the turbulence fluctuations during precipitation events. For clear-air conditions, data from the sonic anemometer, Lyman-α hygrometer, and resistance-wire thermometers must also be analyzed; this is discussed in the following sections.

5.3 METAPE

Program METAPE reads the 100-Hz and 25-Hz micrometeorological data from the Cyber-version data tape, effects cures to the sonic anemometer problems, converts the signals to engineering units, and writes the results to a meteorological working tape. This MET tape is shown in Fig. 2. To this end it also reads the 2.56-s data base disk file and performs whole-tape averages of the temperature, humidity, and Lyman-α voltage counts; these quantities are used in the conversion-to-units for the sonic anemometers and Lyman-α hygrometers. The output to the MET working tape consists of all of the resistance-wire temperatures and Lyman-α humidities written at 100 Hz, as well as the solar flux, sonic wind components, sonic horizontal wind speeds, prop-vane wind speeds and angles written at 25 Hz; all these quantities are written in engineering units. In addition, two flags are written at the 25-Hz rate to the MET working tape; these flags designate whether or not the wind angle at the sonic anemometer lies within the ±45° acceptance range of the sonic-axis configuration. These flags are used in later processing to reject sonic data for wind angles beyond ±45°.

The handling of the sonic data is particularly complex. Program METAPE first reads the sonic components and prop-vane signals from the Cyber-version

data tape. If necessary, the sonic signals are despiked in intervals of 40.96 s of data at a time and then converted to units of meters per second. The prop-vane signals are likewise converted to wind speed in meters per second and to angle in degrees. These results are written to a temporary disk file. Meanwhile the averages in (84) are computed so that the sonic offsets can be determined as discussed in Sec. 4.4. When the entire Cyber-version data tape has been thusly processed, the offsets for the horizontal sonic wind components are obtained from (84). The exhausted Cyber tape is now rewound and read from the beginning to provide the resistance-wire temperatures, Lyman-α humidities, and solar flux. Simultaneously, the temporary disk file is rewound and read to provide the prop-vane speeds and angles already converted to units and the despiked sonic wind components. The sonic offsets are then subtracted from their respective components. Note, however, that determining the sonic offsets by comparison with the prop-vane anemometer is an option that is not used in processing every data tape; alternatively, the offsets from the field log can be used. At the 25-Hz rate the angle between the horizontal wind vector and each sonic axis is calculated and used to correct the sonic components for their wake averaging and to set the flags designating whether or not the wind angle is within the ±45° acceptance range. The wake-averaging correction is given by Kaimal (1980b). Although the wake of one sonic transducer crosses the second sonic axis when the wind angle is beyond ±45°, wind tunnel tests of a related sonic anemometer by Hanafusa et al. (1980) show no effect on the wind measured along this second sonic axis. Using the wake correction gives us confidence in the ±45° acceptance angle. The horizontal sonic components are converted to orthogonal components as described in Sec. 3.2. The horizontal wind speed is calculated from the latter sonic components. Finally the data are written to the MET working tape.

5.4 Stripchart Data Visualization

We now discuss the programs in Fig. 2 labeled GRAPH 2.56-s DATA BASE, STRIPCHART MIL-WAVE, and STRIPCHART MICRO MET. These programs check the data validity and yield the time intervals that we must delete from further processing because of erroneous data. All graphs are produced on microfilm so that the enormous amount of graphical information can be conveniently stored.

In Sec. 5.2 we discussed all of the quantities that program FLATCOPY archived in the 2.56-s data base disk file. The program labeled GRAPH 2.56-s DATA BASE in Fig. 2 makes a graph of each of these quantities versus time during the data run, and one point is plotted for each 2.56 s. In addition it graphs the averaged rain-drop size distribution. It also graphs all of the temperatures on a single graph; these are the four 2.56-s-averaged resistance-wire temperatures and the two dry- and wet-bulb psychrometer temperatures as well as the two Väisälä temperatures. These graphs show us the trends in temperature, humidity, optical C_n^2 and cross wind, rain rate, solar flux, and even barometric pressure. At this point the malfunction of instruments becomes evident. For instance, the fact that the wet bulb in the psychrometer at station 2 is actually dry is evident in session 1, and program METAPE is then commanded to use the humidity from the psychrometer at station 1 to convert the Lyman-α signals from station 2 to physical units. The failure of one of the optical cross-wind and C_n^2 meters is evident in session 1. The trends in temperature reveal whether such trends will dominate temperature variance calculated over the entire data tape.

The program labeled STRIPCHART MIL-WAVE in Fig. 2 produces a stripchart of the six phase differences and four intensities on one microfilm stripchart; 10 s of data is displayed in each frame. A related program can produce a stripchart of the raw mm-wave voltage squares if need be. These stripcharts reveal the presence of phase-lock losses, spikes, step changes, or other problems in the mm-wave data. The time intervals to be skipped in subsequent processing are obtained from these stripcharts. The program also produces printed summaries of the averages, rms, and extrema of the 10 quantities in 100 s intervals. In addition, averages and rms of the 10 quantities are also produced for 20-s intervals and are graphed with the entire data run displayed on single graphs for each of the quantities. These latter graphs display the trends in the mm-wave data.

The program labeled STRIPCHART MICRO MET in Fig. 2 is actually two programs. One produces a single microfilm stripchart for data from the four resistance-wire thermometers and two Lyman-α hygrometers at the rate of 10 s per frame. The second produces stripcharts of the u, v, w components of the sonic anemometers and overplots on these the corresponding u and v components calculated from the prop-vane anemometers; this gives 10 curves per stripchart

at a rate of 20 s per frame. These stripcharts yield the time intervals to be skipped in later processing in case of erroneous data. As with the mm-wave stripcharts, summaries are printed of 100-s averages, rms, and extrema, and 20-s averages and rms are plotted for each quantity to reveal trends. The extrema are used to set the minimum and maximum bins for the probability distribution function calculations.

5.5 PED 2 PAR and MODPARM

Several parameters are needed for the processing of the data. These include times bracketing erroneous data that is to be skipped during processing, the location of spikes, the integration period to be used, etc. In addition, missing block locations obtained from the pedigree file must be provided to the processing programs. A compact file called the parameters file has been defined to retain these parameters for each tape to be processed. Two programs create, modify, and/or display the contents of the parameter file. These are labeled PED 2 PAR and MODPARM in Fig. 2.

The PED 2 PAR program allows two modes of operation. If a non-empty pedigree file is provided, then PED 2 PAR reads the file and extracts from it the timing data identifying missing data blocks. PED 2 PAR searches the parameters file for the times to be skipped during processing and either replaces the missing block times if there is an existing entry or makes a new entry if there is not. In the second mode of operation, PED 2 PAR displays the missing-block data for all data tapes in the parameters file in both absolute time (Greenwich Mean Time) and time relative to the beginning of the tapes.

The MODPARM program allows interactive access to the parameters file. The program first attempts to read the file and verify that the version of the file is at least the minimum needed for the current version of the MODPARM program. MODPARM then presents a menu from which to choose the data tape of interest and those parameters from that tape that the user wishes to inspect or modify. The program then displays the current values of the parameters, and the user is given an opportunity to modify them, thereby altering the parameters file. An example of modifying the parameters file is to enter the beginning and ending times of intervals to be skipped in subsequent processing; identification of such time intervals using our stripcharts was discussed in the previous section.

As shown in Fig. 2, the parameters file is read by the MILDRV program to obtain the parameters needed for performing its processing steps. The output file MILSUMS contains a copy of the values of the parameters file so that a record is available to confirm the validity of parameters used in processing.

5.6 MILDRV and METDRV

The quantities calculated as averages from the mm-wave and micrometeorological data were discussed in Secs. 2.2 to 2.6 and in Sec. 3.3. These quantities are calculated as running sums (rather than averages) in the programs MILDRV and METDRV for the mm-wave and micrometeorological data respectively. The advantages of outputting running sums over time intervals much shorter than a data run will become clear in the next two sections. As shown in Fig. 2, MILDRV reads the data from the Cyber-version tape and outputs the running sums to a disk file called MILSUMS, and METDRV reads the MET tape and outputs to METSUMS (actually METSUMS consists of several distinct disk files). We output the running sums for specified averaging periods; at present we use 25.6-s periods. The one exception is the structure parameters, which we output as averages. Also, the extrema found in each 25.6-s period are recorded in the disk files. The PDFs and JPDFs are also calculated by MILDRV and METDRV and written to the disk files as unnormalized histograms. The number of points summed is also written to these disk files; this number is variable because erroneous data are skipped, and it is different for mm-wave data versus micrometeorological data. This number can differ between micrometeorological stations because only one station may have erroneous data that is skipped, and different statistical quantities from a given station may have different numbers of points summed because sonic data may be dropped due to wind angles outside the ±45° acceptance range and because only some statistics depend on sonic data. The data reduction in MILDRV and METDRV obviously depends on the stripcharts in an essential way because the stripcharts yield the time intervals containing erroneous data that is to be skipped.

It is MILDRV that cures problems in the mm-wave data, as discussed in Sec. 4.3. MILDRV calculates the polynomial-fit correction to all 28 mm-wave channels and synthesizes I_4 for experiment session 1. MILDRV also performs the digital filtering needed to remove erroneous trends in the mm-wave data, and to remove high-frequency noise and noise due to vibration of the I-beam holding the mm-wave receivers.

MILDRV has a second mode of processing in support of the mm-wave fast Fourier transform program, MILFFT. In this mode MILDRV reads the Cyber-version data tape, performs the polynomial-fit correction to the 28 mm-wave channels, synthesizes I_4 if session 1 data are used, and calculates the phase differences. However, in this mode MILDRV does not perform any digital filtering. In so doing, MILDRV uses the parameters file to locate erroneous or lost data and thereby identify all sequential 5.12-s intervals of temporally continuous data. The four intensities and six phase differences are then output to a temporary disk file spanning the entire data tape in blocks of 5.12-s duration. This temporary disk file contains gaps caused by erroneous or lost data. A new 5.12-s block is attempted beginning with the first good datum following erroneous or lost data. Thus the temporal extent of a gap is from the end of one 5.12-s block to the next good datum that is followed by 5.12 s of temporally-continuous and error-free data. The temporary disk file is used by MILFFT.

5.7 Graphing the 25.6-s Statistics

The program labeled GRAPH 25.6-s STATISTICS in Fig. 2 is actually two programs; one graphs the results in MILSUMS and the other those in METSUMS. This program takes the running sums in the disk files, produces averages by dividing by the appropriate number of points summed, converts such quantities as mean squares to more meaningful quantities like central variances, and finally graphs these quantities versus time with one point every 25.6 s per statistic.

At this point these graphs give us a look at the trends in all of our statistics, only a few of which are redundant with the trends visualized in the previous graphing of the 2.56-s data file and the stripcharting. The graphs of the extrema are particularly sensitive to erroneous data that might have eluded us or were wrongly included because the time intervals skipped were incorrect when the data were input to MILDRV or METDRV. If an error is found, the runs of MILDRV and/or METDRV can be repeated.

MILSUMS and METSUMS are repairable files. If an error occurs in a 25.6-s bin, then MILDRV or METDRV can recalculate just this one bin without reprocessing the entire MET or Cyber-version tapes. It is then possible to rewrite the MILSUMS or METSUMS files including the corrected 25.6-s bin.

We check these graphs for statistical stationarity and specify times t_1 to t_2 over which the statistics are sufficiently stationary. A given data tape may have more than one period of stationarity without being stationary as a whole. An extreme example would be a data tape that consists of clear-air data for part of the run but rain data over the remainder of the run. In this case we can use the graphs to specify times t_1 to t_2 for later accumulating the clear-air data and times t_1' to t_2' for accumulating the rain data. By studying these graphs, we can include or exclude data at will in subsequent processing.

5.8 MILRDR and METRDR

Given an interval t_1 to t_2 of stationary statistics as described in the previous section, the programs labeled MILRDR and METRDR on Fig. 2 read the disk files MILSUMS and METSUMS and sum the 25.6-s partial sums from t_1 to t_2 while also summing the numbers of points in each 25.6-s partial sum. These total sums from t_1 to t_2 are converted to averages by dividing by the total number of points summed, and quantities like mean squares are converted to more meaningful quantities like central variance. The PDFs and JPDFs stored for each 25.6 s are summed and then normalized. The extrema of the 25.6-s data are found. The resulting averages (which include such quantities as variances and cross-correlations), the PDFs and JPDFs, and the extrema are identical to those that we could calculate from t_1 to t_2 if we skipped the intermediate step of storing 25.6-s running sums and histograms. The exceptions to this identity are the structure parameters that are stored in the disk file METSUMS as averages. METRDR then averages these 25.6-s-averaged structure parameters from t_1 to t_2. This is actually an advantage for the time-lagged structure parameters because wind speed variability is less on a 25.6-s time interval than from t_1 to t_2, and the relationship between time-lagged and spatial structure parameters relies on wind speed stationarity.

Final normalizations of mm-wave data are performed by MILRDR. For instance, the MCF and fourth moments of the field are converted to their normalized values, as discussed in Secs. 2.5 and 2.6.

Finally, MILRDR and METRDR write the accumulated statistics to the disk file labeled ANSWER FILES in Fig. 2. The answer files may contain only one set of statistics for a given data tape if only one set of times t_1 and t_2 is

specified, but it may contain additional sets if additional times t_1' and t_2' are specified. We have already noted the advantages of data validation and data selection in creating the files METSUMS and MILSUMS of 25.6-s running sums. In addition, this partial sum procedure allows additional processing of differing sets of times t_1 to t_2 to be performed in the distant future without recalculation at the high data rates of 100 Hz and 25 Hz.

5.9 MILFFT and METFFT

Sections 2.9 and 3.9 describe what spectra and cross-spectra are calculated and how this is accomplished for mm-wave and micrometeorological data, respectively. The programs MILFFT and METFFT in Fig. 2 accomplish these transforms and write the averaged results to the answer files. In addition, mm-wave spectra that are not averaged in frequency bins are saved and examined so that noise in the mm-wave intensities and phase differences can be identified for subsequent filtering done by MILDRV in producing the MILSUMS file.

Section 5.6 describes the temporary disk files created by the second mode of MILDRV processing. These files are then read by MILFFT to produce the Fourier transforms. METFFT creates its own analogous disk files for Fourier transformation without a second mode of processing that exists within METDRV. METFFT does not use the parameters file and therefore cannot transform data tapes that have block drops; data tapes preceding tape 12 of session 2 are therefore excluded. However, times bracketing bad data observed on the micrometeorological stripcharts are entered so that bad data do not enter the disk files to be transformed.

In this mode METFFT reads the MET working tape and outputs 5.12-s blocks of temporally-continuous error-free data to four temporary disk files. The choice of these 5.12-s blocks and the temporal extent of gaps between them, if any, is the same as for MILDRV in Sec. 5.6 (except block drops are not considered). There are two disk files for each micrometeorological station. One file holds the 100-Hz data, namely the temperatures from the two resistance-wire thermometers and the Lyman-α hygrometer. The other file holds the 25-Hz data, namely from the three axes of the sonic anemometer and the three 100-Hz quantities averaged by fours to produce 25-Hz data. The temporal integrity of the 100-Hz data derives from any errors within the 100-Hz data, whereas that of the 25-Hz data derives from errors in both the 100-Hz data and the sonic

anemometers and from the wind angle being outside the cone of acceptance for the sonic anemometer.

Once the mm-wave or micrometeorological disk files are created, MILFFT and METFFT use the same versatile Fourier transform program to produce spectra. The data are read from these files in sets of 40.96 s of continuous data, that is, eight 5.12-s blocks that have no gaps beween them. The FFT is performed on a pair of quantities simultaneously and written to another temporary disk file, then another pair is read from the first file, and so on. The user can select a given number of available 40.96-s intervals, and each is Fourier transformed and written to disk. These transforms are read from the disk. The desired power spectra and cross-spectra are formed for each 40.96-s interval and are then averaged together to increase statistical reliability. These spectra still retain their full dependence on frequency and can be graphed to diagnose instrument problems and/or saved in a permanent disk file. Such graphs are especially important for further mm-wave processing because the frequencies and strengths of the various types of noise in the mm-wave data must be identified for subsequent digital filtering before the MILSUMS file is written. Finally, the spectra are averaged into logarithmically spaced frequency bins and graphed as well as written to the answer files.

To produce the low-frequency Fourier transform, the data in the temporary disk file described in Sec. 5.6 are low-pass filtered with a single-pole RC-type filter and then averaged into bins of about 0.6 s such that there are 4096 temporal bins per data tape or per given section of a data tape. The gaps beween the 5.12-s blocks are filled with interpolated values. These data are then Fourier transformed in pairs of quantities, as for the high-frequency FFT, and written to a temporary disk file. When all pairs have been transformed, the desired power spectra and cross-spectra are formed and corrected for the effects of low-pass-filter and bin averaging. These spectra are then averaged into logarithmically spaced frequency bins, graphed, and written to the answer files.

5.10 Using the Answer Files

The set of all answer files from all data tapes provides a very versatile data base for interpreting the data and preparing publications. This flexibility is the desired end product alluded to in Sec. 1. Computer programs can

be written and modified to present the reduced data in any graphical or tabular manner desired. For instance, programs can be written to plot all the MCFs versus antenna spacing for the clear-air data, with one curve for each desired refractive-structure parameter value, then alternatively plotted versus antenna spacing scaled by a theoretical wave coherence length. Alternatively, these clear-air MCFs could be plotted for various values of surface-layer stability rather than refractive-structure-parameter values. The MCFs from turbulence, rain, fog, and snow data could all be plotted on a single graph for comparison by accessing the answer files for these diverse meteorological conditions. One could tabulate all of the temperature and humidity structure parameters and cross-structure parameters from the various different methods of calculating them (spatial, time-lagged, optical scintillation) to search for data consistency or errors. Clearly these examples are insignificant compared with the myriad relationships that could be investigated using the answer files.

5.11 Archiving of Disk Files

The Cyber-version data tape and MET tape are, of course, magnetic tapes and can therefore be stored for further processing as long as desired or practical. The various disk files in Fig. 2 cannot reside on disk indefinitely because of disk-storage costs. Consequently, the 2.56-s data base file as well as the MILSUMS and METSUMS files are dumped to magnetic tape and deleted from disk after the answer files are made. Thus these files can be returned to disk if further data processing is desired in the future. Likewise, the answer files are dumped to magnetic tape and deleted from disk when desired. It is expected that the magnetic tapes for the answer files will be retained indefinitely.

6. REDUCED MILLIMETER-WAVE AND MICROMETEOROLOGICAL DATA

6.1 Introduction

As an example of our data processing results, we present reduced data from the answer files of data tapes 20, 22 to 25, and 27 of experiment session 1. It should be remembered that the intensity at antenna 4 is synthesized, as

discussed in Sec. 4.3. The probability distribution functions are normalized to unit area under a curve connecting the histogram peaks. That is, the sum of the probability over all bins is made equal to the number of bins divided by the range of the independent variable.

6.2 Tabular Results

Tables 4 and 5 are mm-wave statistics averaged over the whole of session 1 for tapes 24 and 20, respectively. In interpreting these results one should keep in mind that the root-mean-square (rms) intensity decreased by 30% in an almost linear fashion over the duration of tape 20 data, with a much less dramatic change in rms phase differences. On the other hand, tape 24 had nearly constant rms intensities and rms phase differences.

As expected, the intensity variance is much less than unity. Ideally all four antennas should give equal variances. Agreement is good, but the synthesized intensity at antenna 4 gives the least agreement for tape 24. The minimum and maximum intensities are normalized by dividing by the mean intensity. Table 4 shows that over the whole of tape 24 the intensities swung from about 0.5 to greater than 1.5 of the mean intensity.

The phase variances in these tables differ from one antenna pair to the next, as they should because of the differing antenna separations. The minimum and maximum phase differences likewise show corresponding variability. As seen in Table 4, the largest observed phase differences exceeded 3 radians. The mixed intensity-difference and phase-difference correlation given in Eq. (7) is very much smaller than either the intensity variance or phase-difference variance. Thus amplitude and phase are relatively uncorrelated. The phase-type figures of merit are much smaller than any of the phase-difference variances; this verifies the consistency of the phase-difference measurements.

The ρ-type figures of merit in Tables 4 and 5 suggest that the MCF should not be trusted to better than about 5% accuracy. In Tables 4 and 5 the ρ type and Σ type are close to unity, as desired, even for antenna pairs 3, 5, and 6, which use the synthesized intensity at antenna 4. The variances of both ρ-type and Σ-type figures of merit show that there is very little temporal variation about the mean values of these figures of merit.

Table 4.--Millimeter-wave statistics from the answer files obtained by averaging all of tape 24 of session 1, July 1983

Intensity Statistics

Antenna number	Intensity variance	Normalized minimum intensity	Normalized maximum intensity
1	0.0210	0.540	1.70
2	0.0219	0.523	1.74
3	0.0216	0.423	1.75
4	0.0287	0.433	1.74

Phase Difference Statistics

Antenna pair	Phase-difference variance	Minimum phase difference	Maximum phase difference	Eq. (7)
1	0.081	-1.32	1.08	-7.12 (-6)
2	0.315	-2.46	2.37	-8.54 (-6)
3	0.703	-3.25	3.09	-1.50 (-5)
4	0.193	-1.67	1.75	-7.90 (-6)
5	0.563	-3.24	2.87	-9.86 (-6)
6	0.408	-2.47	2.29	-4.87 (-6)

Figures of Merit

Antenna pair	ρ type	ρ-type variance	Σ type	Σ-type variance
1	1.07	2.85 (-5)	1.10	4.66 (-4)
2	1.05	4.48 (-4)	1.03	7.41 (-4)
3	1.02	5.85 (-5)	0.934	3.13 (-3)
4	1.03	2.57 (-4)	1.01	2.06 (-3)
5	1.00	3.61 (-5)	0.944	4.18 (-3)
6	0.976	8.43 (-5)	0.869	1.75 (-3)

Antenna numbers	Phase type (a variance)
1&2&4	8.16 (-4)
1&3&5	2.51 (-3)
2&3&6	1.36 (-3)
4&5&6	9.24 (-4)
1&3&4&6	2.49 (-3)

Note: Numbers in parentheses indicate powers of 10.

Table 5.--Millimeter-wave statistics from the answer files obtained by averaging all of tape 20 of session 1, July 1983

Intensity Statistics

Antenna number	Intensity variance	Normalized minimum intensity	Normalized maximum intensity
1	0.0059	0.694	1.34
2	0.0046	0.716	1.26
3	0.0066	0.638	1.43
4	0.0066	0.635	1.34

Phase Difference Statistics

Antenna pair	Phase-difference variance	Minimum phase difference	Maximum phase difference	Eq. (7)
1	0.024	-0.58	0.68	-2.06 (-6)
2	0.104	-1.32	1.19	-3.59 (-6)
3	0.193	-1.50	1.74	-1.50 (-6)
4	0.063	-1.13	1.02	-2.18 (-6)
5	0.163	-1.54	1.41	-7.09 (-7)
6	0.131	-1.41	1.38	-1.45 (-6)

Figures of Merit

Antenna pair	ρ type	ρ-type variance	Σ type	Σ-type variance
1	0.979	1.27 (-4)	0.89	1.28 (-3)
2	1.00	7.10 (-5)	0.88	1.16 (-3)
3	0.964	1.10 (-4)	0.81	1.53 (-3)
4	1.04	1.71 (-4)	1.06	3.02 (-4)
5	1.01	1.96 (-4)	1.02	1.75 (-3)
6	1.02	4.34 (-4)	0.99	6.05 (-3)

Antenna numbers	Phase type (a variance)
1&2&4	3.00 (-4)
1&3&5	5.83 (-4)
2&3&6	4.99 (-4)
4&5&6	8.57 (-4)
1&3&4&6	4.93 (-4)

Note: Numbers in parentheses indicate powers of 10.

Table 6 is a summary of the micrometeorological data from tape 24, which were taken at about 11:30 a.m, July 1983. These averages were obtained from 480 s into the run to its end at 2400 s. The values of the structure parameters imply that the humidity structure parameter overwhelmingly dominates the calculated mm-wave refractive-index structure parameter. The values of temperature structure parameters from optical and fine-wire instruments are in excellent agreement. The small but nonzero value of the mean of the cross-stream wind component is a measure of the inaccuracy of determining the true streamwise direction.

6.3 Graphical Results

Figure 3 shows the intensity probability distribution function (PDF) for antenna 1 for session 1, tape 24. Gaussian and lognormal PDFs having the same mean and variance are also plotted. There is little difference between the Gaussian and lognormal PDFs for such small values of variance. However, the data are clearly skewed and more nearly follow the lognormal PDF, as is expected theoretically.

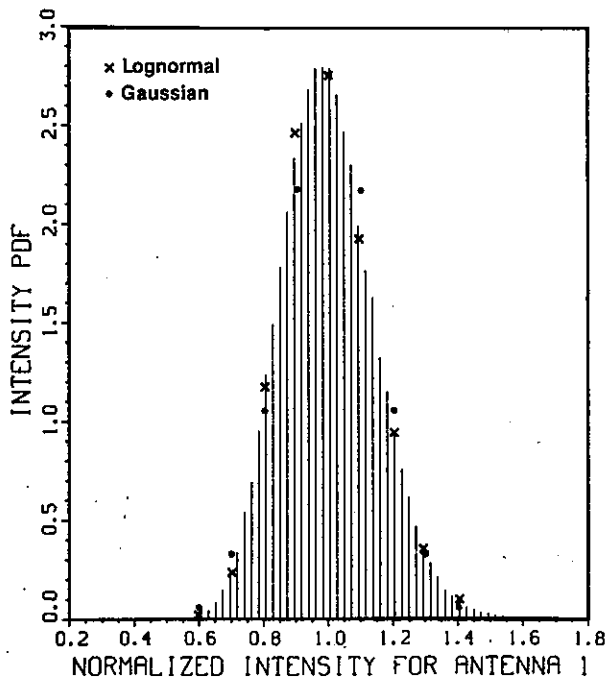

Figure 3.--Probability distribution function of intensity for antenna 1, session 1, tape 24, July 1983. Gaussian and lognormal distributions are also shown. Normalized intensity is scaled to unit mean value. The distribution is normalized to unit area under the histogram.

Table 6.--Summary of micrometeorological data from tape 24, taken at 11:30 a.m., July 1983

Average Values	
Humidity	19 g/m^3
Temperature	32°C
Wind speed	5.3 m/s
Wind angle	10°
Pressure	993 mb
Solar flux	94% of full sun
Wind stress	$-0.14\ (m/s)^2$
Humidity flux	$0.1\ (g/m^2)/s$
Temperature flux	0.03°C m/s
Stability	-0.03

Square Roots of Variances	
Humidity	0.72 g/m^3
Temperature	0.35°C
Wind speed	1.2 m/s
Wind angle	11°
Streamwise wind component	1.1 m/s
Cross-stream wind component	1.0 m/s
Vertical wind component	0.54 m/s

Structure Parameters	
C_n^2 from optical scintillometers	$2 \times 10^{-13}\ m^{-2/3}$
C_T^2 from optical C_n^2	$0.03°C^2\ m^{-2/3}$
C_T^2 from resistance wires	$0.03°C^2\ m^{-2/3}$
C_q^2 from Lyman-α hygrometers	$0.2\ (g/m^3)^2\ m^{-2/3}$
C_{Tq} from resistance wires and Lyman-α hygrometers	$0.075°C\ (g/m^3)\ m^{-2/3}$
C_n^2 for radio frequencies*	$5.9 \times 10^{-12}\ m^{-2/3}$

*Obtained from Eq. (79), using C_T^2, C_q^2, and C_{Tq} from the resistance-wire thermometer and Lyman-α hygrometer with A_T and A_q obtained from the radio refractive-index equation.

Figure 4 shows the phase-difference PDF for antenna pair 4 of session 1, tape 24. A Gaussian PDF having the same mean and variance is also plotted. Clearly the phase difference is Gaussian, as is expected theoretically.

Figure 5 shows the structure function of phase versus receiver separation. Tape 20 corresponds to the 6:50 p.m. data and tapes 22 to 27 correspond to times 8:40 a.m. to 3:50 p.m. of the following day. The six receiver separations correspond to the six antenna pairs. At a given receiver separation, the value of the structure function of phase is just the phase-difference variance for the corresponding antenna pair. Also plotted is a theoretical prediction for the 6:50 p.m. data assuming a 14-m horizontal outer scale.

Figure 6 shows the modulus of the mutual coherence function; the 3:50 p.m. data of tape 27 are not included. Since the intensity PDF is lognormal and the phase-difference PDF is Gaussian, it follows theoretically that the MCF should equal exp(-D/2) where D is the sum of the structure functions of log-amplitude and phase; this relationship is satisfied to within 0.5% in the mm-wave data. Although not shown, the imaginary part of the MCF is very much smaller than the real part, as is expected theoretically.

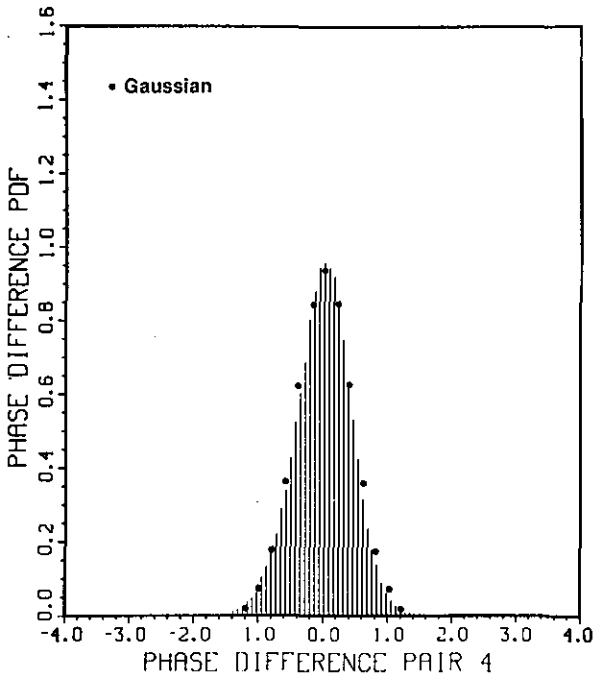

Figure 4.--Probability distribution of phase difference in radians for antenna pair 4, session 1, tape 24, July 1983. A Gaussian distribution is also shown. This distribution is normalized to unit area under the histogram.

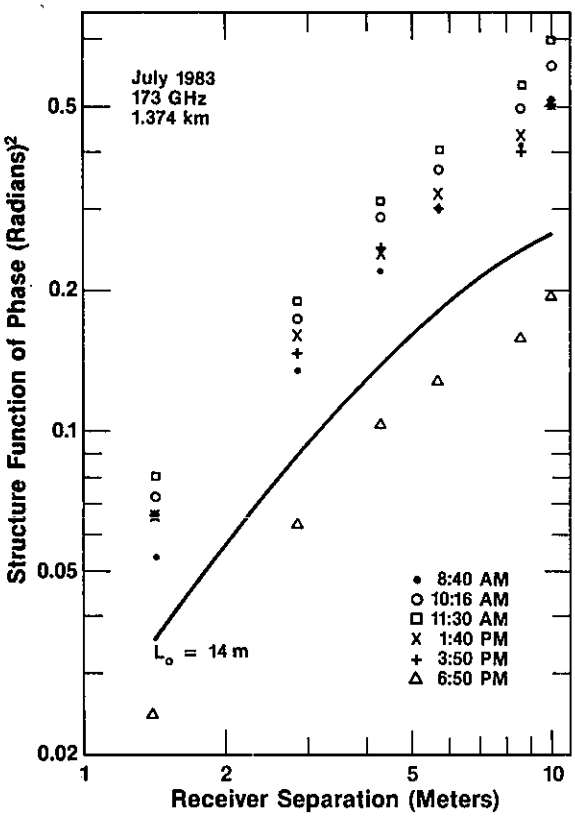

Figure 5.--The structure function of phase. The solid line represents a theoretical prediction for the 6:50 p.m. data, assuming a 14-m horizontal outer scale.

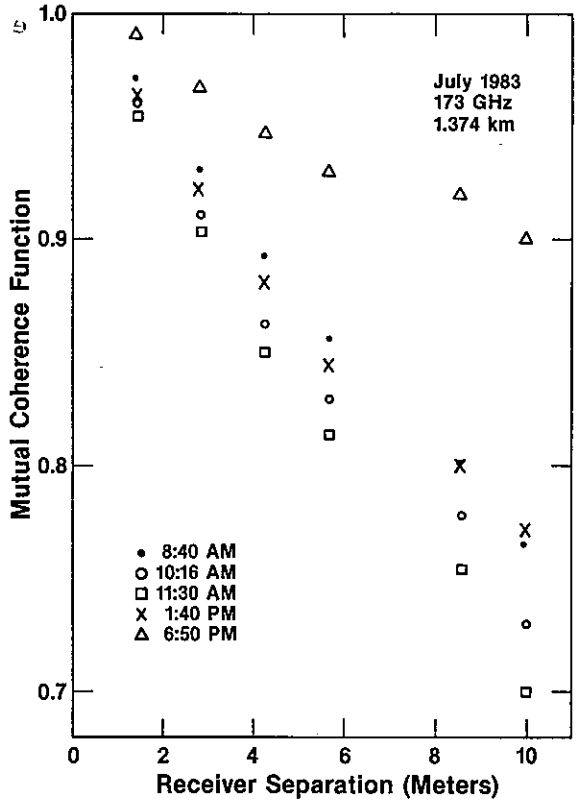

Figure 6.--The modulus of the mutual coherence function.

Figure 7 shows the normalized intensity variance plotted versus its theoretical formula for inertial-range turbulence. Here, C_n^2 is deduced from the micrometeorological data. The straight line shows agreement with theory. Lack of agreement could be caused by the outer scale of turbulence or inaccurate calibration of the Lyman-α hygrometer.

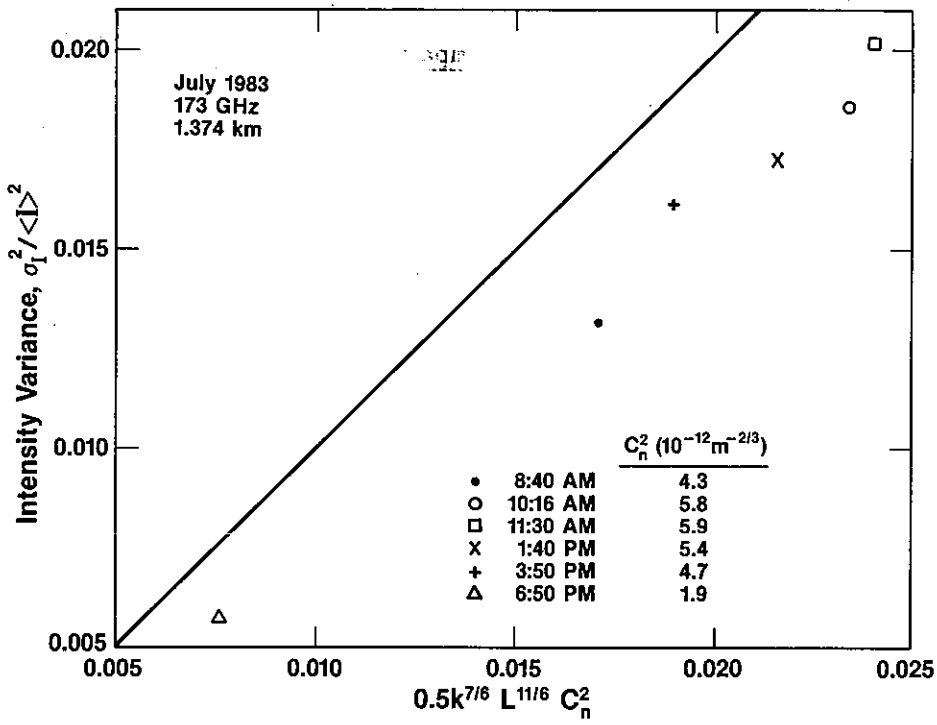

Figure 7.--The normalized variance of intensity versus its inertial-range formula. The straight line shows theoretical calculations.

7. ACKNOWLEDGMENTS

This work was supported by the Army Research Office under MIPR 122-85. We thank William Moninger for his careful review of the manuscript.

8. REFERENCES

Hanafusa, T., Y. Kobori, and Y. Mitsuta, 1980. Single-head sonic anemometer-thermometer. The Boulder Low-Level Intercomparison Experiment, Report No. 2, NOAA/ERL, Boulder, CO, 7-13.

Kaimal, J. C., 1980a. Sonic anemometers. In Air-Sea Interaction: Instruments and Methods. Plenum Press, New York, 81-96.

Kaimal, J. C., 1980b. BAO sensors for wind, temperature, and humidity profiling. The Boulder Low-Level Intercomparison Experiment, Report No. 2, NOAA/ERL, Boulder, CO, 1-6.

Schmitt, K. F., C. A. Friehe, and C. H. Gibson, 1978. Humidity sensitivity of atmospheric temperature sensors by salt contamination. J. Phys. Oceanogr. 8:151-161.

☆ U.S. GOVERNMENT PRINTING OFFICE: 1985--576-000 / 20030